Experimentally validated modeling of the temperature distribution and the distortion during the Fused Filament Fabrication process

Anton Trofimov[a], Jérémy Le Pavic[b], Sébastien Pautard[b], Daniel Therriault[a], Martin Lévesque[a,*]

[a] *Laboratory for Multiscale Mechanics, Polytechnique Montréal, Montréal, QC H3C3A7, Canada*
[b] *Safran Composites, a technology platform of Safran Tech, Itteville, 91760, France*

Abstract

This paper presents the numerical approach to compute process-induced temperature distribution and distortion in Polylactic Acid (PLA) parts manufactured using the Fused Filament Fabrication (FFF) process. Thermal simulations are performed first to compute the time-dependent temperature distribution which is then input as solution-independent boundary condition into a mechanical simulation to compute warpage of the manufactured part. The developed procedure used experimentally measured process parameters and was experimentally verified at each step of the simulation.

The thermal step in the simulation workflow was experimentally validated using thermography yielding quantitative predictions for 25 out of 27 considered points with the highest accuracy of $< 1°$C. To verify mechanical step, the computed process-induced distortions were compared against those measured with an optical 3D scanner. The developed procedure yielded qualitative and, in some cases, quantitative predictions of process-induced geometrical distortions.

Keywords: Fused Filament Fabrication, Polylactic Acid, additive manufacturing, Finite Element Method, 3D printing, process simulation

1. Introduction

The Fused Filament Fabrication (FFF) process consists in extruding a molten polymer-based filament through a nozzle that follows a predefined path. The FFF process involves temperature gradients that may source the residual stresses built up generating undesired part distortion [1]. Residual stresses and distortions mainly result from the polymer evolution from a semi-molten to a solid state throughout the manufacturing process [2, 3].

The FFF process parameters are currently tailored through costly and time consuming trials and errors [4]. Accurate predictive simulation tools could be used to simulate the process and hence optimize its parameters to limit part distortion, or to account for it to reach the target shape on the first attempt. The FFF process involves multi-physical phenomena like solidification, heat transfer and mechanical loads. All of these features are interconnected with the process parameters and influence the overall part performance [5]. Therefore, a simulation procedure requires a robust constitutive thermomechanical model of an extruded material, realistic representation of the process parameters and experimental verification of predictions at each step of the analysis.

The Finite Element Method (FEM) with progressive element activation allows to simulate the FFF process using various constitutive models of a polymer, and accounting for the process

*Corresponding author
Email address: martin.levesque@polymtl.ca (Martin Lévesque)

parameters such as the tool-path pattern, the nozzle velocity, the extrusion temperature, the layer thickness and the filament width, the temperature and the air flow inside the chamber etc. [6].

One of the first full 3D FEM model to simulate FFF process was developed by Zhang et al. [7]. The authors investigated the effect of the tool-path pattern on the FFF process. Zhang et al. conducted a thermoelastic analysis relying on a stepwise activation of elements following the extrusion path history to predict the formation of residual stresses in a regular Acrylonitrile Butadiene Styrene (ABS) plate. The polymer was assumed to be linearly elastic with temperature-dependent thermal properties estimated from the literature. The extrusion temperature and the temperature inside the chamber were extracted from the printer settings. The air flow inside the chamber as well as convection parameters were estimated from the literature. The authors showed that the tool-path pattern influenced the magnitude and the distribution of the computed residual stresses. The same model and simulation framework were used in [8] to predict the effect of other process parameters like nozzle velocity, layer thickness and filament width on the final residual stress state and resulting distortion. The authors concluded that the nozzle velocity has the most significant influence on a part distortion, followed by the layer thickness. Cattenone et al. [9] simulated the influence of the constitutive models on the FFF process of an ABS bridge-like part. The extrusion temperature and the temperature inside the chamber were extracted from the printer settings. The air flow inside the chamber as well as convection parameters were estimated from the literature. To validate predictions, the authors measured displacements along global x and z axes using a laser scanner and compared them against simulated values at each test point. The authors reported that the use of temperature dependant Young's modulus and yield stress along with constant thermal properties resulted in an average discrepancy of 12% between the predicted and measured distortion.

The available literature shows that FEM-based models are capable of qualitative predictions simulating the interactions between the process parameters and part's distortion. To reach quantitative predictions, the simulation model must be fed with measured, instead of assumed, process parameters and an experimental validation of thermal step of simulation.

This paper presents the warpage simulation procedure combining measured process parameters and experimentally verified thermal step of the procedure. For the first time such a comprehensive computation procedure is used to predict distortion of the complex PLA parts. The work suggests the hierarchy of the process parameters importance and emphasizes associated difficulties. It creates a robust procedure that can be followed for further improvements in numerical and experimental works. The paper is organized as follows: Section 2 recalls background information on the FFF simulation framework and thermomechanical constitutive models. This section defines the necessary information to follow our paper. The FFF of PLA parts, thermomechanical properties, measurement of the process parameters, thermographic and distortion measurements are described in Section 3. Section 4 provides the workflow to simulate the FFF process. Section 5 demonstrates comparison of the thermal and mechanical predictions against the experimental data. Discussion and conclusions are given in Sections 6 and 7, respectively.

2. Background information

Courter et al.[10], Cattenone et al. [9] and Barocio et al. [11] proposed the workflow schematized in Figure 1 to simulate the FFF process. The Figure shows that the the part's geometry is defined as a CAD model which is converted to the set of FFF process parameters summarized in a G-code. The G-code is decoded to extract the time dependent coordinates of filaments center-lines, their cross-section area and to compute the activation times for each finite element describing the

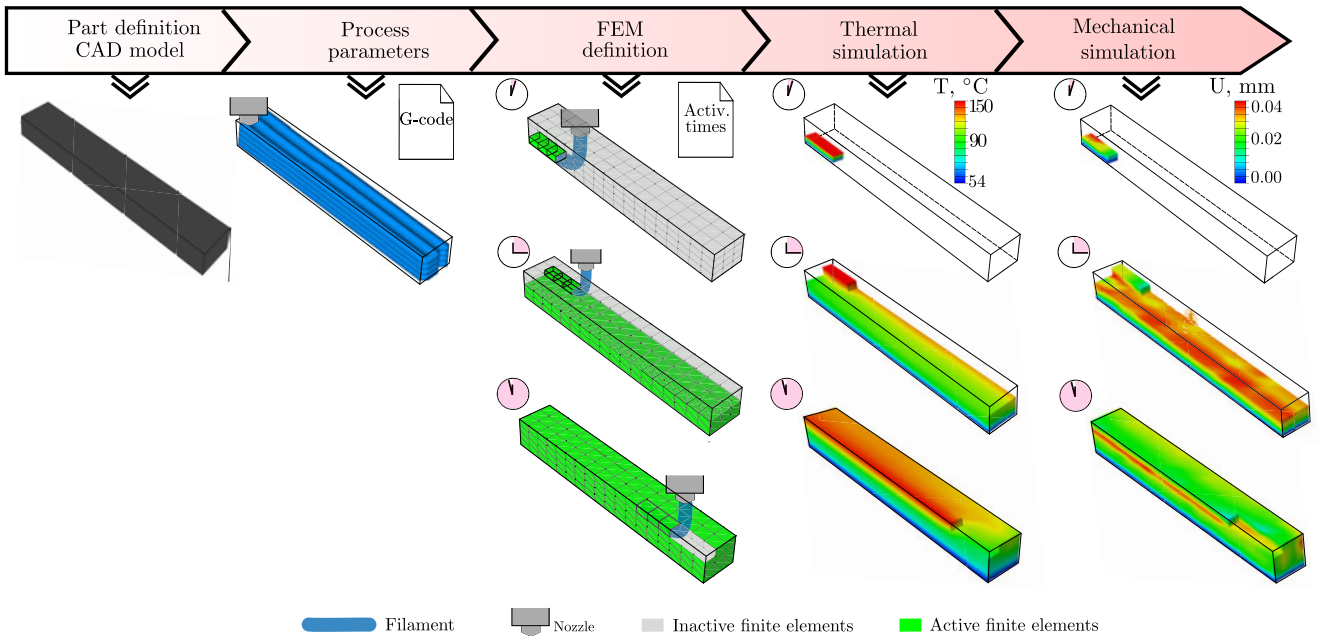

Figure 1: Schematic representation of the workflow to simulate the FFF process, illustrated for a rectangular beam. The part's geometry is defined as a CAD model that is converted to the set of FFF process parameters summarized in G-code. The G-code is decoded to extract the time dependent coordinates of filaments center-lines, their cross-section area and compute the activation times for each finite element describing the voxelized volume of a part. The activation times are used to simulate the FFF process with the progressive element activation approach. The thermal simulations are performed first to compute the time-dependent temperature distribution. The temperature distribution is then input a solution-independent boundary condition into a mechanical simulation to compute the residual stresses and the deformation of the manufactured part. This image was created based on the workflows found in [9, 10, 11].

voxelized volume of a part. The activation times are used to simulate the FFF process with the progressive element activation approach [12]. Thermal simulations are performed first to compute the time-dependent temperature distribution. The temperature distribution is then input as solution-independent boundary condition into a mechanical simulation to compute the residual stresses and the deformation of the manufactured part.

2.1. Progressive element activation

The general procedure to compute finite element activation times was summarized in [12] and is schematized in Figure 2. The Figure shows that the time dependent x, y and z coordinates of a filament center-line computed from the G-code is used to define the print path. The filament elliptic cross-section is assumed to be constant and idealized by a rectangle whose dimensions correspond to the ellipse's semi-axes. This rectangle marches along the print path to compute activation times when the center of an element falls within it.

2.2. Thermal model for heat transfer analysis of the FFF process

The schematic representation of the heat transfer analysis is presented in Figure 3 and is inspired from the work of Costa et al. [13]. Figure 3 presents two domains: the extruded filament Ω_f and the print bed Ω_b. Authors in [13] suggested to account for six main phenomena: (1) convection from the filament to the surrounding; (2) conduction between the the filament overlays; (3) conduction between filament and the print bed; (4) constant heating of the bed; (5) convection from the bed to the surrounding and (6) heat flux from the extruder.

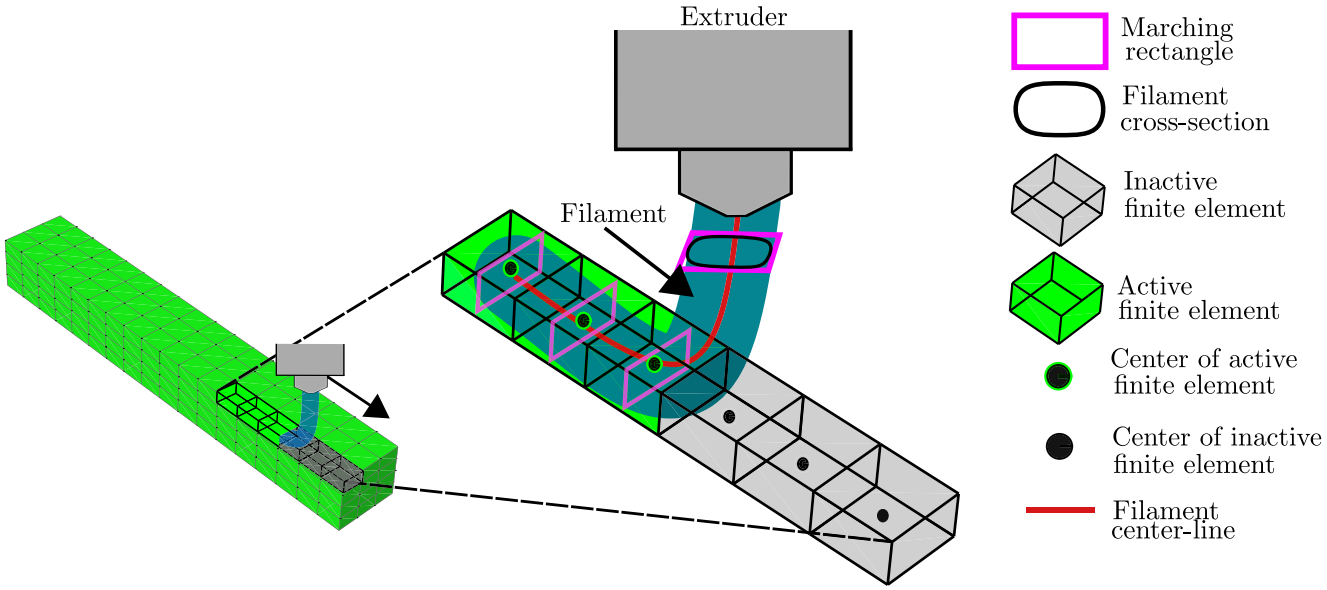

Figure 2: Schematic representation of the general procedure to compute finite element activation times. The filament elliptic cross-sections are assumed to be constant and idealized by a rectangle whose sides have the dimensions of the ellipse's semi-axes. This rectangle marches along the print path to compute activation times when the center of an element falls within it. This Figure is inspired from the works of [9].

For isotropic constituents, the classical 3D heat transfer equations for the extruded filament and the print bed are [14]:

$$\rho_f c_p^f \frac{\partial T}{\partial t} = \nabla \cdot \Big(k_f \nabla T \Big), \tag{1a}$$

$$\rho_b c_p^b \frac{\partial T}{\partial t} = \nabla \cdot \Big(k_b \nabla T \Big), \tag{1b}$$

where T is the temperature, t is the time, ∇ is the vector differential operator, $\cdot$ is the dot product, ρ_f and ρ_b are respectively the filament and the print bed densities, c_p^f and c_p^b are respectively the filament and print bed specific heat capacities, k_f and k_b are respectively the filament and print bed thermal conductivities. The initial conditions of the problem are given by:

$$T(\boldsymbol{x}, 0) = T_f, \boldsymbol{x} \in \Omega_f \tag{2a}$$

$$T(\boldsymbol{x}, 0) = T_b, \boldsymbol{x} \in \Omega_b, \tag{2b}$$

where $\boldsymbol{x}$ is the position vector, T_f and T_b are respectively the initial temperatures of the filament and the print bed.

The extruded filament is subjected to the boundary conditions

$$k_f \frac{\partial T}{\partial \boldsymbol{n}} + q_c^{fs} + q_r^{ef} = 0, \boldsymbol{x} \in S_f(t), \tag{3}$$

where $\boldsymbol{n}$ is the outward normal vector to the surface of the filament, $S_f(t)$ is the external surface of the filament that increases during the deposition, q_c^{fs} is the convection heat flux from the filament to the surrounding and q_r^{ef} is the radiation heat flux from the extruder to the filament defined as:

$$q_c^{fs} = h_f(T - T_s), \tag{4a}$$

$$q_r^{ef} = \beta\epsilon(T_e^4 - T_s^4), \tag{4b}$$

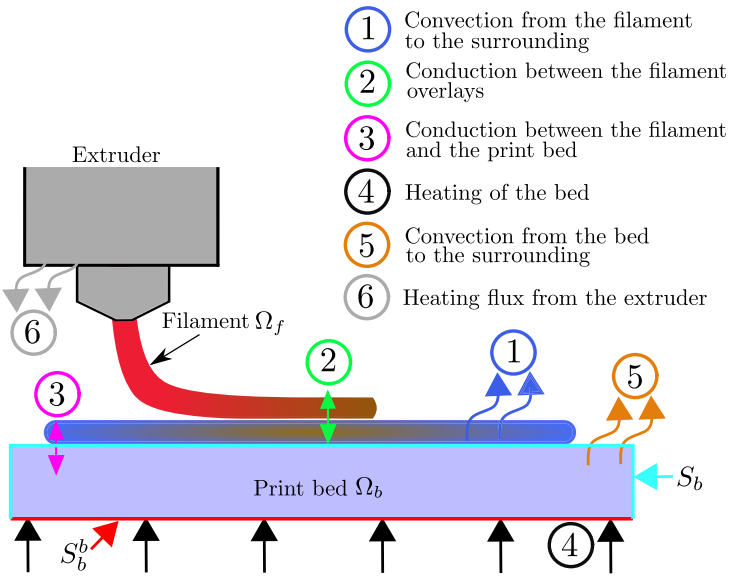

Figure 3: Schematic representation of a numerical model to simulate the heat transfer during the FFF process. The simulation assumes two domains: the extruded filament Ω_f and print bed Ω_b. The six main heat transfer mechanisms include: (1) convection from the filament to the surrounding; (2) conduction between the filament overlays; (3) conduction between the filament and the print bed; (4) constant heating of the bed; (5) convection from the bed to the surrounding and (6) heat flux from the extruder. The Figure is inspired from the work Costa et al. [13].

where h_f is the heat transfer coefficient of the filament, T_s is the temperature of the surrounding, β is the Stephan-Boltzmann constant and ϵ is the emissivity of the extruder.

The print bed is subjected to the following boundary conditions:

$$T(\boldsymbol{x}, t) = T_b, \boldsymbol{x} \in S_b^b, \tag{5a}$$

$$k_b \frac{\partial T}{\partial \boldsymbol{n}} + q_c^{bs} + q_r^{eb} = 0, \boldsymbol{x} \in S_b, \tag{5b}$$

where T_b is the temperature of the bed, S_b^b is the bottom surface of the bed, $\boldsymbol{n}$ is the normal vector to the surface of the bed, S_b is the external surface of the bed excluding the bottom surface S_b^b, q_c^{bs} is the convection heat flux from the bed to the surrounding and q_r^{eb} is the radiation heat flux from the extruder to the bed. q_c^{bs} and q_r^{eb} are defined as:

$$q_c^{bs} = h_b(T - T_s), \tag{6a}$$

$$q_r^{eb} = \beta\epsilon(T_e^4 - T_s^4), \tag{6b}$$

where h_b is the heat transfer coefficient of the bed.

Implementing a thermal simulation requires the following parameters: (1) the thermal properties of the filament and the print bed (see Equation 1); (2) the T_f and T_b (Equations 2 and 5); (3) the ϵ, $S_f(t)$ (see Equation 3); (4) the h_f, h_b, T_s and T_e (see Equations 4, 6).

As it was emphasized by Brenken et al. [6], a realistic representation of the material's properties and process parameters is required for accurate implementation. Therefore, we further provide details about the model parameters.

Regarding parameters in (1), Farah et al.[15] demonstrated that in the range of temperatures between $\sim 50°C$ and $\sim 190°C$, PLA's thermal properties can change by up to $\sim 75\%$. Therefore, temperature dependence of PLA's thermal properties needs to be accounted for. In contrast, Zhang et al. [7] suggested that the thermal properties of the bed can be assumed as constant.

The recommended nozzle temperature for PLA's extrusion is 210°C [16]. However, Prajapati et.al. [17] showed that during manufacturing, the filament's temperature at deposition (T_f) may decrease by up to 10% and therefore the value of T_f requires experimental validation.

Bejan et al. [18] and Costa et al. [19] suggested that the heat transfer coefficients with the surroundings were dependent on the process parameters such as the air flow and temperature inside the chamber. Costa et al. [19] used Hilpert's data to identify the filament's heat transfer coefficient as:

$$h_f = \frac{Nu_d k_{air}}{d_f}, \tag{7}$$

where d_f is the filament's diameter, k_{air} is the air thermal conductivity and Nu_d is the Nusselt number defined by:

$$Nu_d = C_H Re^{n_h} Pr^{1/3}, \tag{8}$$

where C_H and n_H are empirical constants estimated from Hilpert's data [18], Pr is the Prandtl number at the environmental temperature and Re is the Reynolds number defined as:

$$Re = \frac{\rho_{air} v_{air} d_f}{\mu_{air}}, \tag{9}$$

where μ_{air} is the air viscosity at T_s, v_{air} is the air speed and ρ_{air} is the air specific weight. The use of Equation 7 requires knowledge of the physical constants of the air that can be found in [20] and the process-specific parameters such as the filament cross-section, the air speed and the surrounding temperature. Costa et al. [19] reported that without an additional cooling system and at the room temperature, the air speed may range between 0.1 and 0.5 m/s and the surrounding temperature may range between 40 and 65°C, depending on the distance to the extruder.

2.3. Mechanical model for structural analysis of the FFF process

Cattenone et al. [9] inputted the computed time-dependent temperature distribution as solution-independent conditions into a thermo-elasto-plastic constitutive model to compute the total strain response $\boldsymbol{\varepsilon}^{tot}$ defined as:

$$\boldsymbol{\varepsilon}^{tot} = \boldsymbol{\varepsilon}^{e} + \boldsymbol{\varepsilon}^{pl} + \boldsymbol{\varepsilon}^{t}, \tag{10}$$

where $\boldsymbol{\varepsilon}^{e}$ are elastic strains, $\boldsymbol{\varepsilon}^{pl}$ are plastic strains and $\boldsymbol{\varepsilon}^{t}$ are the non-mechanical strains associated to the thermal dilatation defined by Hill [21] as:

$$\boldsymbol{\varepsilon}^{e} = \mathbf{S}_f(T) : \boldsymbol{\sigma}, \tag{11a}$$

$$d\boldsymbol{\varepsilon}^{pl} = \lambda \boldsymbol{\sigma}^{\boldsymbol{dev}}, \tag{11b}$$

$$\boldsymbol{\varepsilon}^{t} = \boldsymbol{\alpha}_f(T) \Delta T, \tag{11c}$$

where $\boldsymbol{\sigma}$ is the second order stress tensor, $\mathbf{S}_f(T)$ is the fourth order temperature-dependent elastic compliance tensor of the filament, $d\boldsymbol{\varepsilon}^{pl}$ is the plastic strain increment, $\boldsymbol{\sigma}^{\boldsymbol{dev}}$ is the deviatoric part of the stress tensor, $\boldsymbol{\alpha}(T)$ is the temperature dependent second order coefficient of thermal expansion tensor and λ is the plastic flow [21] such that:

$$\lambda = \begin{cases} 0, & \sigma_{VM} \leq \sigma_y(T) \\ > 0, & \sigma_{VM} > \sigma_y(T), \end{cases} \tag{12}$$

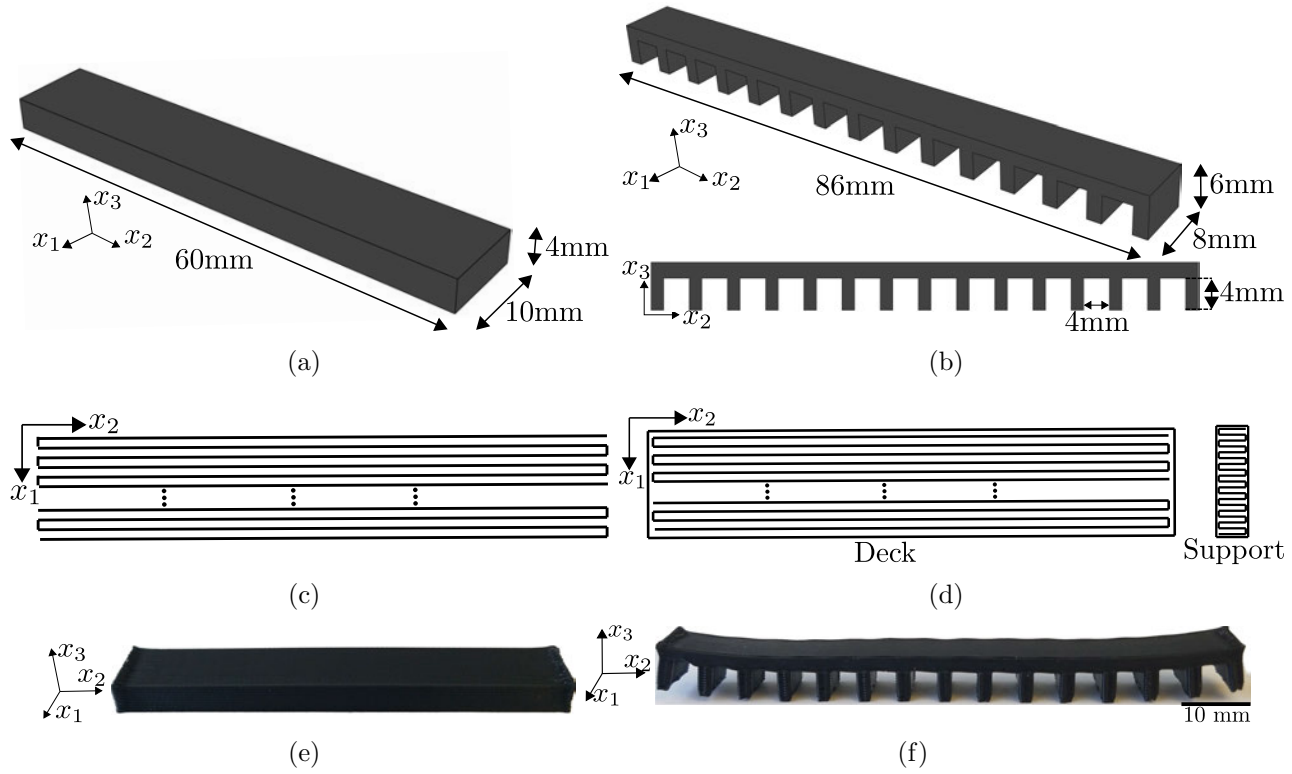

Figure 4: Manufacturing of the PLA specimens using the FFF process: (a) 3D CAD design of a regular plate; (b) 3D CAD design of a bridge-like structure and side view; (c) print path of the regular plate part; (d) print path of the bridge-like part; (e) final manufactured regular plate; (f) final manufactured bridge-like part.

where $\sigma_{VM} = \sqrt{\frac{3}{2}\boldsymbol{\sigma}^{dev} : \boldsymbol{\sigma}^{dev}}$ is the von-Mises stress and $\sigma_y(T)$ is the temperature dependent yield stress.

Implementing the mechanical model of Equation 11 requires the following parameters: (1) $\mathbf{S}_f(T)$ (see Equation 11a); (2) the $\sigma_y(T)$ (see Equation 11b); (3) $\boldsymbol{\alpha}(T)$ (see Equation 11c).

The mechanical properties of PLA reported in the publicly available literature exhibits considerable scatter (for example, Espinach et al. [22] report a Young's modulus at room temperature being equal to $\sim$ 3.3GPa, while Zhou et al. [23] report it being equal to $\sim$ 2.9GPa, while Song et al. [24] report it being equal to $\sim$ 4GPa). Moreover, [23, 22] have shown that PLA's properties are temperature dependent. For example, Espinach et al. [22] showed that the Young's modulus of PLA dropped by $\sim$ 25% at $\sim$ 65°C (the material's reported glass transition temperature T_g is of $\sim$ 65°C) and almost simultaneously reduced to $<$ 1% of its room temperature value after T_g. Similar behaviour was observed for the yield stress in [23]. Espinach et al. [22] showed that the coefficient of thermal expansion (CTE) at $\sim$ 100°C increased by $\sim$ 100% of its value measured at $\sim$ 35°C.

3. Materials and methods

3.1. Manufacturing

A Raise3D Premium PLA filament was used to manufacture specimens with a Raise3D Pro2 FFF printer [16]. Figure 4 schematizes the chosen geometries that were sliced using Simplify3D to build the required G-codes. Figures 4(c), 4(d) show the print path of a typical layer for both parts. Both parts had an infill of 100%, a layer thickness of 0.2 mm and were printed with a nozzle

Table 1: Properties of the PLA and the print bed that were measured experimentally and were taken from the works of [15, 22, 24]. Note that, for the print bed, only the thermal properties are given since it was not modeled in the mechanical simulations

T, °C	**PLA**							**Print bed**		
	E, $\times 10^6$Pa [22]	ν [22]	σ_y, $\times 10^6$Pa [22]	α_f, 1/°C [24]	k_f, W/mK [15]	c_p^f, $\times 10^3$J/kgK [15]	ρ_f, $\times 10^3$kg/m^3 [15]	k_b, W/mK	c_p^b, $\times 10^3$J/kgK	ρ_b, $\times 10^3$kg/m^3
25	1860	0.36	25.0	7.9×10^{-5}	0.11	1.59	1.25	1.5	0.5	8
30										
40	1727		18.9							
50	1603		15.3							
60	1000		11.7							
70	300		8.2							
80	50									
90	10		7.0							
100	1			14.7×10^{-5}	0.19	1.95				
150	1									

having a diameter of 0.4 mm at 210°C while the temperature of the bed was programmed to 60°C. For both parts, the first layer deposition speed was almost half speed as that of the rest of the layers to increase adhesion. A Raise3D Pro2 printer has three cooling fans: one to cool down the nozzle and two to cool down the filament. The two fans cooling the filament were disabled during the process to reduce the number of unknowns in the simulation (see Section 2.2 for further details). A planar and regular plate geometry (Fig. 4(a)) with a simple nozzle path allowing for accurate thermography measurements was used to validate the heat transfer simulation. A typical bridge-like structure promoting warpage (Fig. 4(b)) was chosen to validate distortion predictions. A hot extruder (210°C) following complex deposition path was blocking the filament at many times, which made thermal measurements during bridge-like part manufacturing highly unreliable. Since the process parameters during polymer's deposition for the regular plate and the bridge-like structures were the same, we validated the regular plate geometry thermal model to simulate the thermal step of the FFF process simulation for the bridge-like part. After manufacturing, the bridge-like part was cooled down by natural convection for one minute which led to an average temperature of ~ 60°C at the surface of the deck and then released from the flexible print bed to let it free standing while cooling by natural convection to room temperature (25°C). Figures 4(e), 4(f) show the manufactured specimens.

3.2. Thermomechanical properties

The thermal properties of PLA were taken from the work of [15]. The Young's modulus and yield stress of PLA at room temperature were measured using an MTS servo-hydraulic machine 609.24A-01 with an axial extensometer MTS 632.26C-20. We decreased the mechanical properties measured at room temperature with the function reported by Espinach et al. [22]. The thermal properties of the print bed were computed as per the inverse approach detailed in Appendix A. The mechanical properties of the print bed were not required as the part was assumed to be perfectly attached to it. The assumed thermomechancial and thermal properties of the PLA and the print bed are given in Table 1.

The air properties required to compute heat transfer coefficients (Eq. 7) were reported in [20, 25] and are summarized in Table 2.

3.3. Measurement of the process parameters

The print bed temperature (T_b) and the temperature of the filament at the nozzle tip (T_f) were measured using a FLIR IR T420 camera in a video mode. The IR camera featured a 320×240

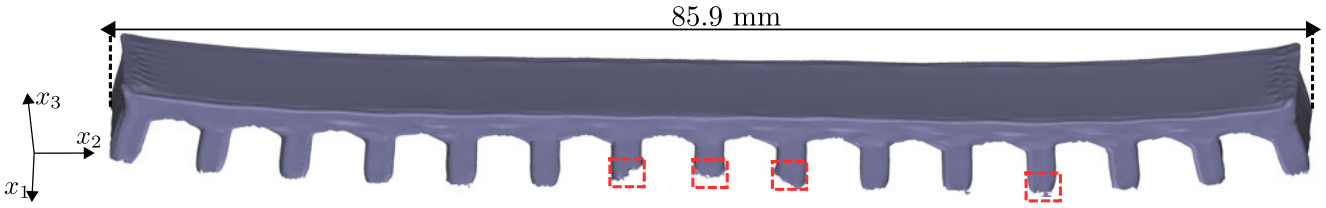

Figure 5: Digitized surface of the bridge-like part studied in this work, with the highlighted areas of poor reconstruction.

pixels 60 Hz infrared detector having a 0.04 °C thermal sensitivity and a −20 to 650°C temperature measurement range. The temperature of the surrounding (T_s) air around the nozzle and inside the printer enclosure was measured during and after the FFF process with type K thermocouples.

3.4. Measurement of the thermal fields during the FFF in a planar and regular plate

In our paper, we focus on the comparison of the layer's temperature fields throughout the process. Therefore, 1D measurements with thermocouples or optical fibers with Bragg gratings were not valid alternatives. To measure thermal fields, a measurement device must be installed within a close distance from the nozzle and at an angle from which the nozzle will not block the readings. Moreover, it must be installed inside the print chamber as the printer's acrylic glass cover was not transparent which would have altered IR readings.

Therefore, the temperature evolution during the FFF process was measured with a FLIR IR T420 camera which was small enough to fit in our print chamber, allowed convenient placing near the nozzle at a proper angle and offered a thermal fields measurements in a video mode. Post processing of the measurements was conducted in MATLAB 2018a using "VideoReader" built-in function which converts a video to a set of images. These images contained pixels of the size (0.32 mm × 0.24 mm), which is different from the size of the finite elements (0.4 mm × 0.4 mm) that were used in this work. The the experimental data was linearly interpolated to pixels having the same dimensions as the finite elements for comparison purposes.

3.5. Measurement of the distortion in a bridge-like part

The external surfaces of the bridge-like specimen were reconstructed using the 3D optical scanner ATOS Core with the maximum resolution of 0.08 mm. During the process, a user takes a set pictures of the specimen attached to a rotary table at various positions and post-processes the results to generate a digital model.

The surfaces of the bridge supports were poorly reproduced, which can be explained by their small dimensions. Also, the length of supports in the middle of the part were not reconstructed properly since they were attached to the rotary table using the blue tack. Figure 5 illustrates the reconstructed model and highlights regions emphasizing the artefacts. Figure 5 will be used as a reference to compare numerical predictions and experimental measurements (Section 5).

4. FFF process simulation methodology

We implemented the workflow presented in Figure 1 to simulate the FFF process. The G-code containing process parameters was decoded using a custom `python` code. The decoded output was processed with an in-house `python` procedure to compute the activation times of each finite element of the voxelized CAD geometry, as discussed in Section 2.1 and reported in Appendix B. The obtained activation times were programmed into ABAQUS's UEPACTIVATIONVOL

Table 2: Parameters that were used to simulate the thermal fields during the FFF

	Deposition	Cooling	Source of a value
k_{air}, W/mK	0.028	0.025	[20, 25]
μ_{air}, $\times 10^{-5}$kg/ms	2.008	1.849	[20, 25]
ρ_{air}, kg/m^3	1.059	1.184	[20, 25]
v_{air}, m/s	0.1	0.1	[9]
T_s, °C	60	25	Measured, Section 3.3
T_b, °C	52	52	Measured, Section 3.3
T_e, °C	150	-	Measured, Section 3.3
h_f, W/m^{2}K	71	67	Computed, Eq. 7
h_b, W/m^{2}K	5	5	Computed, Eq. 7
ϵ	0.92	-	[17]
β, $\times 10^{-8}$ kg/s^{3}K^4	5.671	-	[26]

subroutine and input into FEM thermal and mechanical simulations to implement progressive element activation. We used the full activation of the elements. The boundary conditions for the thermal and mechanical problems were specified on inactivate elements and were not applied until the element was activated.

4.1. Thermal simulation of the thermal fields during the FFF in a planar and regular plate

The thermal simulation of the FFF process included three stages with different boundary conditions: (1) deposition of the filaments, (2) cooling of the part on the flexible print bed and (3) free standing of the part.

Deposition

Figure 6(a) schematizes the FEM heat transfer setup during deposition. Opaque parts (extruder and filament) were not modeled. The radiation from the extruder was implemented using ABAQUS's DFLUX subroutine.

The measured surrounding temperature, the air properties required to compute heat transfer coefficients (Eq. 7), the parameters of initial Eqs. 2a, 2b and boundary conditions Eqs. 4b, 4a, 5a, along with fundamental constants, are listed in Table 2.

Cooling

Figure 6(b) schematizes the heat transfer FEM setup during cooling. The measured surrounding temperature, the air properties required to compute heat transfer coefficients (Eq. 7) and the parameters of boundary conditions Eqs.4b, 4a, 5a, along with fundamental constants, are listed in Table 2.

Free standing

Figure 6(c) schematizes the heat transfer FEM setup during free standing. At this step, all parameters were identical to those from the cooling phase. The difference was in the print bed which was removed and, thus, the part's newly released surface was subjected to convection.

FEM model and convergence analysis

During the deposition phase, the initial temperature at the element activation should be equal or close to T_f. However, it was observed that the simulation time step Δt influenced T_f. For example,

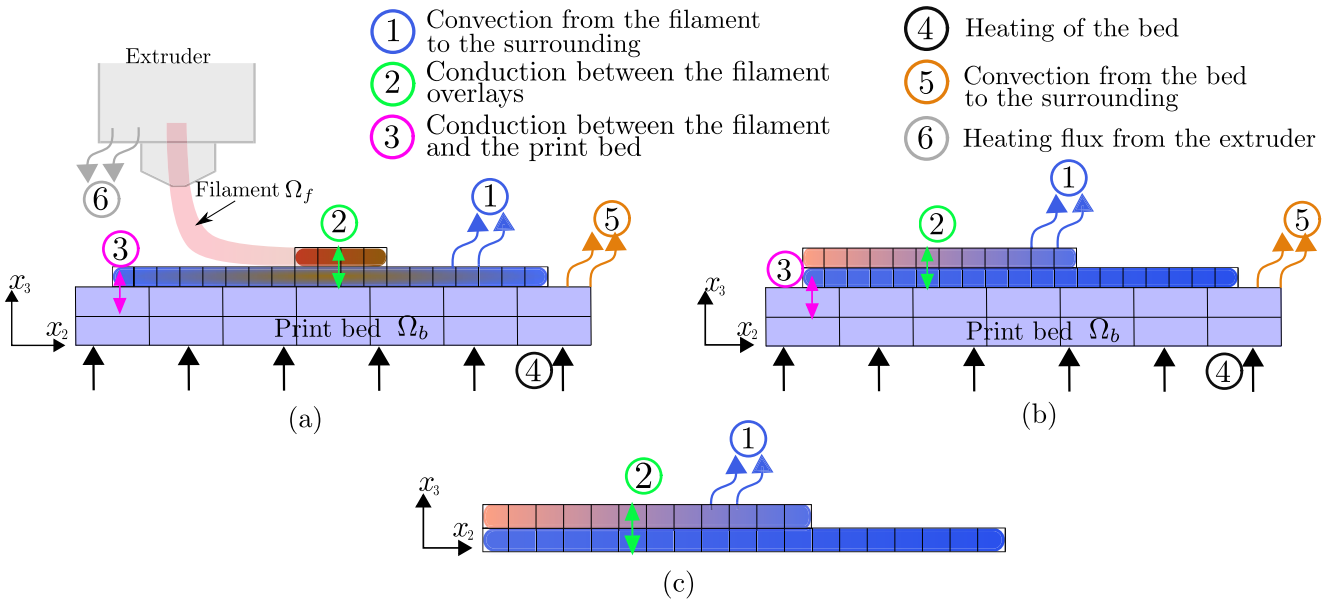

Figure 6: Schematic 2D representation of the 3D FEM thermal simulation steps and the corresponding thermal phenomena during: (a) deposition; (b) cooling and (c) free standing. Opaque parts (extruder and filament) were not modeled directly. The grid represents finite elements in 2D

.

if we assume the cooling rate of a PLA filament being 50°C/s, to capture a temperature change of 1°C, we need to have $\Delta t \leq 0.02$ s. Small Δt improves the accuracy of the simulation but also increases the computational burden. A convergence analysis, based on the lowest computed initial temperature at the element activation, was performed to identify the optimal Δt for simulating the deposition stage. A convergence analysis was performed for the part in Figure 4(a) and the results were assumed to be valid for the part in Figure 4(b).

We performed five thermal simulations of the deposition stage with linear 8-node brick elements (DC3D8) where the element size along x_1 and x_2 was equal to the nozzle diameter (0.4 mm) and along x_3 was equal to the layer thickness (0.2 mm), while Δt varied. The meshing strategy resulted in 74 999 elements. The dimensions of the print bed along x_1 and x_2 were assumed to be twice as large as that of the considered part while the dimension along x_3 was equal to 1 mm. The print bed was discretized with 10 302 DC3D8 elements. The lowest computed activation temperature against the time step and CPU time are presented in Figure 7(b). We deemed that a time step of $\Delta t = 0.01$ s yielded sufficiently accurate results because increasing the computational time drastically, only changes the temperature by less than 5%.

The bridge-like part (Figure 4(b)) was discretized with elements having the same type and size and resulted in 67 400 elements while the associated print bed consisted of 8 156 elements.

For both parts, the cooling phase was of 1 min and the free standing phase was of 5 min. The time step in both phases was of $\Delta t = 0.1$ s.

4.2. Sensitivity analysis of the computed thermal fields to the thermal transfer parameters

We assumed that the air speed and the surrounding temperature were uniform to simplify the measurement of these process parameters. Moreover, Eq. 7 is a correlation formula that assumes an ideal geometrical representation of the filament. In addition, the bed temperature was measured before the FFF process. Real process parameters may deviate from these assumptions and, therefore, we performed a sensitivity analysis.

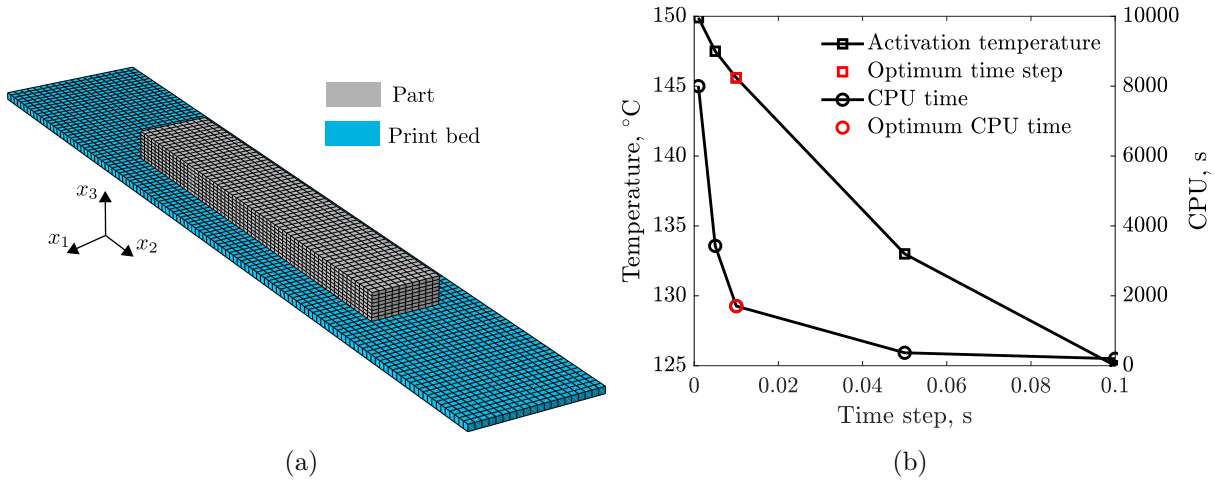

(a) (b)

Figure 7: Schematic representation of the key elements of the convergence study for simulating the FFF process: (a) the FEM mesh of the part presented in Figure 4(a) and the print bed; (b) the lowest computed temperature at the finite element activation against the time step and CPU time.

Sensitivity of the computed thermal fields to the radiation from the extruder

We repeated the simulation procedure described in Section 4.1 and with the parameters listed in the Table 2 without the radiation heat transfer mechanism detailed in Section 2.2 and depicted in Figure 4.1 as mechanism #6.

Sensitivity of the computed thermal fields to the air speed v_{air}

We repeated the simulation procedure described in Section 4.1 with the air speed values of $v_{air} = 0.05,\ 0.15$ m/s, which are different by 50% from the original value of $v_{air} = 0.1$ m/s. The heat transfer coefficients of the filament and the bed were updated accordingly using Eq. 7 and became $h_f|_{v_{air}=0.05} = 57.1$ W/m^{2}K, $h_f|_{v_{air}=0.15} = 82.0$ W/m^{2}K, $h_b|_{v_{air}=0.05} = 3.9$ W/m^{2}K, $h_b|_{v_{air}=0.15} = 6.6$ W/m^{2}K, respectively.

Sensitivity of the computed thermal fields to the temperature of the surrounding T_s

We repeated the simulation procedure described in Section 4.1 with the surrounding temperature values during the deposition phase of $T_s = 30,\ 90$ °C which are different by 50% from the original value of $T_s = 60$ °C. The heat transfer coefficients of the filament and the bed were updated accordingly using Eq. 7 and became $h_f|_{T_s=30} = 70.3$ W/m^{2}K, $h_f|_{T_s=90} = 73.3$ W/m^{2}K, $h_b|_{T_s=30} = 5.4$ W/m^{2}K, $h_b|_{T_s=90} = 5.5$ W/m^{2}K, respectively.

Sensitivity of the computed thermal fields to the temperature of the bed T_b

We repeated the simulation procedure described in Section 4.1 with the bed temperature values of $T_b = 26$ and 78 °C which are different by 50% from the original value of $T_b = 52$ °C.

4.3. Mechanical simulation

The mechanical simulation of the FFF process included three stages with different boundary conditions: (1) deposition, (2) cooling and (3) free standing.

During the deposition stage, the part was subjected to:

- Fully constrained nodal displacements ($u_{x_1}, u_{x_2}, u_{x_3} = 0$) on the S_b^b depicted in Figure 8(a);
- A temperature distribution from the thermal simulation of the deposition phase.

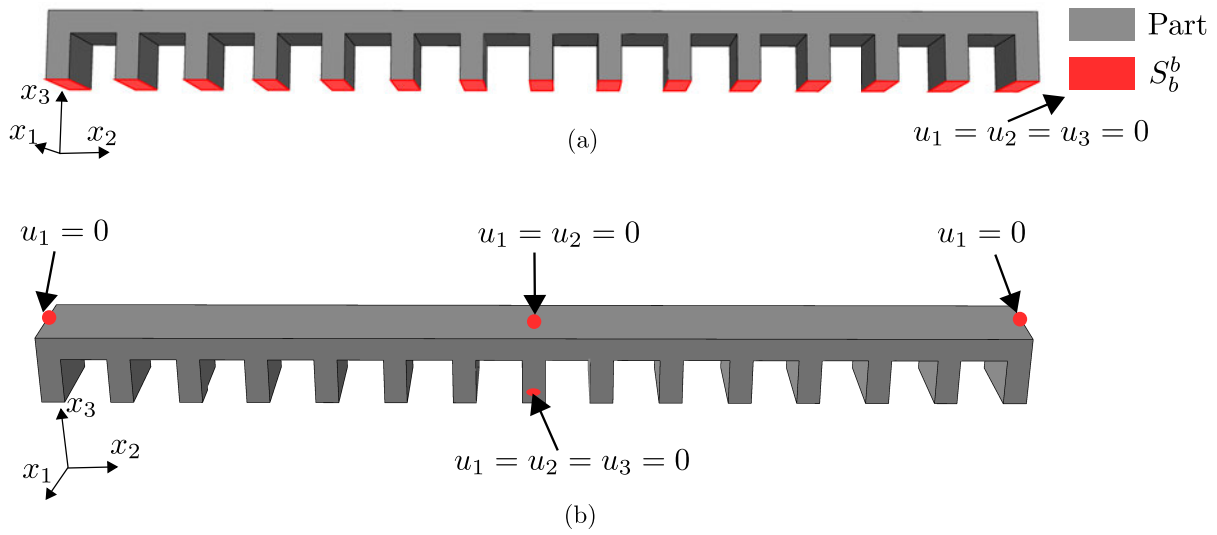

Figure 8: Schematic boundaries conditions for: (a) the deposition and the cooling, and (b) the free standing stages for the mechanical simulation of a bridge-like part presented in Figure 4(b).

During the cooling stage, the part was subjected to:

- Fully constrained nodal displacements ($u_{x_1}, u_{x_2}, u_{x_3} = 0$) on the S_b^b depicted in Figure 8(a);
- A temperature distribution from the thermal simulation of the cooling phase.

During the free standing stage, the part was subjected to:

- Free standing conditions as shown in Figure 8(b) that constrained rigid body motions;
- A temperature distribution from the thermal simulation of the free standing phase.

FEM model and convergence analysis

A convergence analysis, based on the computed distortion, was performed to identify the optimal number of elements.

We performed three mechanical simulations with quadratic 20-node brick elements (C3D20R) where the element size along x_1 and x_2 was equal to the nozzle diameter (0.4mm), while along x_3 varied to have one (0.2mm), two (0.1mm) and four (0.05mm) elements per filament's cross-section. The print bed was discretized with 10 302 elements (C3D8) elements. The average relative difference of the warpage predictions with respect to those of the finest mesh ($\sim$ 261 560 elements and 1 175 601 degrees of freedom) against CPU time and the number of degrees of freedom are presented in Figure 9. We deemed that one element per filament's cross-section yielded sufficiently accurate results because increasing the computational time by $\sim$5 and $\sim$45 times, only changes the average relative difference of the warpage by $\sim 2\%$ and $\sim 3.2\%$, respectively, and the maximum warpage by less than 1%. This result can be explained by the use of non-linear elements.

The bridge-like geometry presented in Figure 4(b) was discretized with 67 400 elements (C3D20R) having 312 301 degrees of freedom. Similarly to the thermal simulations, the deposition stage was simulated with $\Delta t = 0.01$s while cooling and free standing stages were computed with $\Delta t = 0.1$s.

5. Results

This section presents raw results while analysis is given in Section 6.

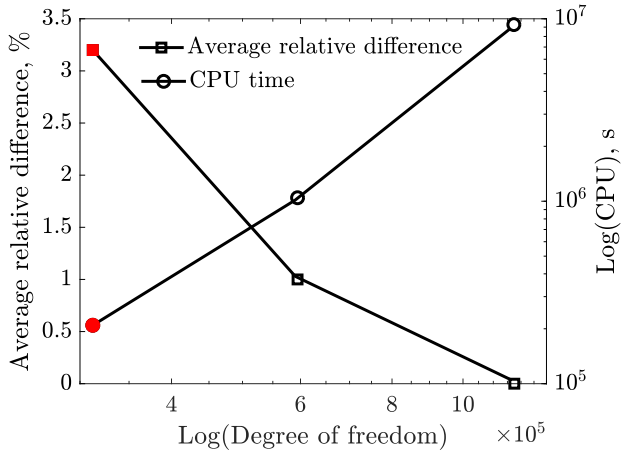

Figure 9: Convergence study for the mechanical simulation of the FFF process showing the relative average warpage difference (%) predicted by the FEM models consisting of 312 301, 594 486 and 1 175 601 degrees of freedom with respect to those of the finest mesh (1 175 601 degrees of freedom) plotted against CPU time and the number of degrees of freedom. The optimal choice is displayed with solid red markers and consisted of 312 301 degrees of freedom because increasing the computational time by ∼5 and ∼45 times, only changes the average relative difference of the warpage by $\sim 2\%$ and $\sim 3.2\%$, respectively.

5.1. Comparison between the thermal fields computed numerically and those experimentally measured

The predicted and experimentally measured temperature fields were compared for the regular plate geometry shown in Figure 4(a) at the first, the tenth (middle) and the twentieth (last) layers. Since the thickness of the finite elements was equal to the thickness of a deposited layer, the number of layers in the numerical model was the same as in the manufactured specimen. The experimentally measured and predicted temperature at the 27 points shown in Figure 10 were compared. It was found that the readings close to the upper (along x_2) edge were influenced by the radiation from the extruder and, therefore, points # 3,6,9,12,15,18,21,24 and 27 were distanced from the edge. The temperature at a considered point was recorded for the period covering the instant the material was deposited until the time the line containing this point was manufactured. For example, the first deposited line at layer #1 contained points #1, 2 and 3.The temperature at point #1 was recorded between the time the material was deposited at point #1 until deposition along this line was finished. This strategy reduced the time span for the comparison, however, it ensured that the readings were not affected by the radiation from the extruder when printing the next line.

Figures 11(a)-(k) compare the numerically predicted temperature against that experimentally measured at the points presented in Figure 10. Note that, since the first layer deposition speed was almost twice lower, when compared to that of the rest of the layers (see Section 3.1), the time span on the Figures 11(a-c) is larger than on the Figures 11(d-k). Figure 11 shows that the FE simulation qualitatively approximated the experimental response at all considered points and reproduced the evolution of the temperature during the deposition, for the different layers. At the first layer, the material was deposited on the bed generating higher temperature gradients, as compared to the subsequent layers, which were successfully captured by the numerical predictions. The proposed numerical approach quantitatively estimated the temperature evolution at all considered points, except #4 and 7, with the lowest and the highest absolute errors being $< 1°C$ and $\sim 10°C$, respectively. The maximum discrepancy was of $\sim 24°C$ and was encountered at the middle section of the curves at points #4 and 7 located on the first layer.

Figure 12(a)(a) shows the temperature distribution computed numerically and that experimen-

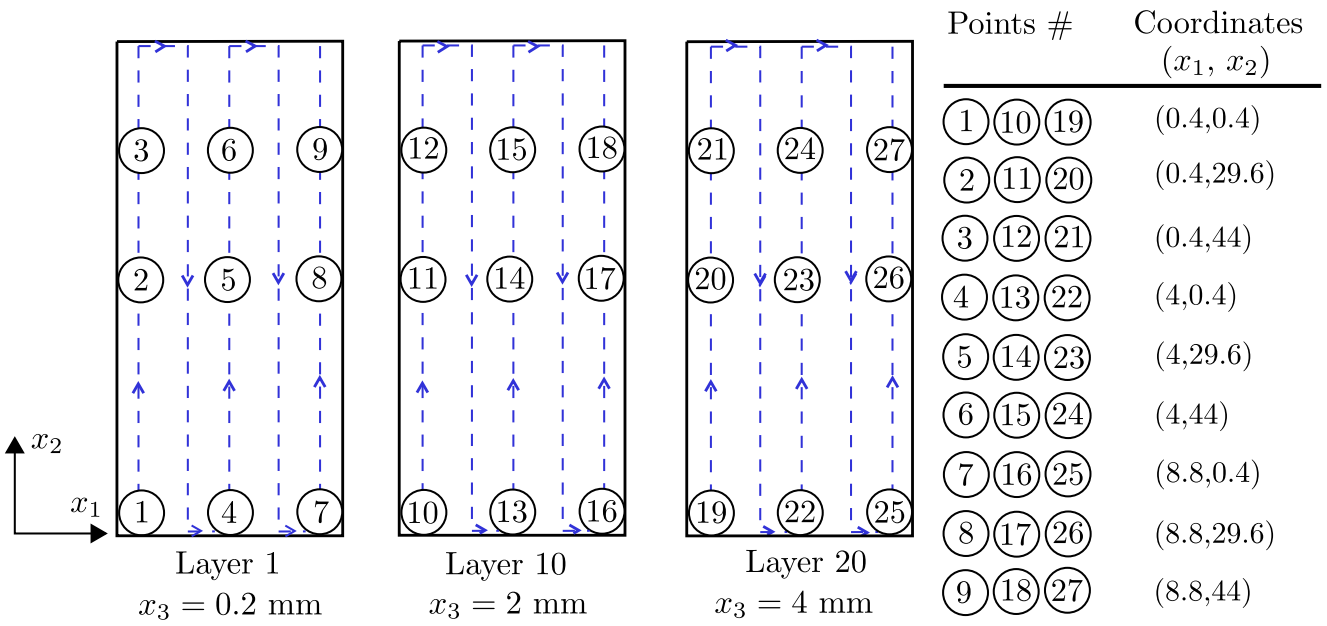

Figure 10: Schematic representation of the points at which the experimentally measured and predicted temperatures were compared. 9 points per layer were considered at the first, the tenth (middle) and the twentieth (last) layers. The dashed line schematizes the path of the nozzle.

tally measured at the end of deposition of the first, the tenth (middle) and the twentieth (last) layers. The FEM simulation predicts more localized temperature distribution, when compared to the measured data for all layers. Also, it can be seen that the FE simulation was able to approximate the evolution of temperature gradients capturing the slower cooling at higher layers.

Figure 12(a)(b) presents the absolute error between the temperature distribution computed numerically and that experimentally measured at the end of deposition of the first, the tenth (middle) and the twentieth (last) layers. It was found that the highest discrepancy of ~ 75°C occurred near or at the extruder location. At the same time, for the rest of the areas the discrepancy was no more that ~ 10°C.

5.2. Comparison between the thermal fields computed using process parameters from Table 2 and those simulated using process parameters assumed in the sensitivity study

The simulated temperature fields were compared for the regular plate geometry shown in Figure 4(a) at the 1st, the 10th and the 19th points depicted in Figure 10. The number of data points was selected to reduce the load of this paper.

Figure 13 presents the temperature distribution at the considered points computed with the parameters listed in Table 2 against those simulated with the parameters presented in Section 4.2.

The presence of the radiation mechanism (mechanism #6 in Figure 6) had negligible effect on the predictions at all points.

The increase of the T_b from its original value of 52°C to the 76°C led to the maximum absolute discrepancies of $\sim 19,\ 3$ and 6°C at the points #1, 10 and 19, respectively. The decrease of the T_b from its original value of 52°C to the 26°C resulted in the maximum absolute errors of $\sim 15,\ 2$ and 3°C at the points #1, 10 and 19, respectively.

The increase of the v_{air} from its original value of 0.1m/s to the 0.15m/s led to the maximum absolute discrepancies of $\sim 10,\ 2$ and 3°C at the points #1, 10 and 19, respectively. The decrease of the v_{air} from its original value of 0.1m/s to the 0.05m/s resulted in the maximum absolute errors of $\sim 9,\ 3$ and 6°C at the points #1, 10 and 19, respectively.

The increase of the T_s from its original value of 60°C to the 90°C led to the maximum absolute discrepancy of $\sim 7,\ 14$ and 12°C at the points #1, 10 and 19, respectively. The decrease of the T_s from its original value of 60°C to the 30°C resulted in the maximum absolute error of $\sim 11,\ 13$ and 11°C at the points #1, 10 and 19, respectively.

5.3. Comparison between the distortion computed numerically and that experimentally measured

The CAD model of the specimen was set as a reference with zero distortions and referred as the nominal. This model was uploaded to the GOM Inspection Software which resulted in the mesh containing the elements referred as nominal. The file with digitized surfaces of the specimen was also (Section 3) uploaded to the same software which generated the surface mesh consisting of the elements referred as actual. Due to the difference in spatial orientations, we aligned the reference and the reconstructed surfaces. The GOM Inspection Software associated actual and nominal elements to compute distortions. We repeated the procedure for the simulated surface to compute distortions resulted from the FFF process modelling. Due to the limitations of the part's reconstruction (Section 3) we only compared the distortion of the deck.

Figure 14(a) compares the computed distortion contour plot while Figure 14(b) shows the measured distortion of the manufactured part's deck. As it was expected, the distortion contour plots showed a high level of symmetry with respect to the center of the deck. A minor deviation from the symmetry could be explained by the non-uniform cooling resulting from the FFF process and by the discrepancies in the reconstruction and alignment procedures. The experimentally measured distortion contour pattern was qualitatively captured by the simulation. The experimental data showed larger area of small distortion and a more steep increase in the deformation close to the edges (along the x_2), when compared to the simulated data. The maximum absolute values of distortion were found at the corners of the deck along x_2 and they were positive for both the numerical analysis and the experimental data. The minimum absolute values of distortion were obtained at the center of the deck for both the computed and the experimental data. The displacements are also plotted along the 'Middle line' illustrated in Figure 14(c) to allow for a more detailed comparison.

Figure 14(c) compares the computed distortion against that experimentally measured along the 'Middle line', depicted in Figures 14(a,b). The simulation procedure was able to approximate the maximum distortion with a relative error of $\sim 8\%$. The worst discrepancies between the predictions and measurements were approximately in the areas of 15 mm - 25 mm and 60 mm - 70 mm.

Figure 15(a) shows the experimentally measured deformation of the bridge supports. Most of the supports were found to be inclined towards the center of the structure for both the numerical analysis and the experimental data. The FE simulation was able to approximate the maximum inclination angle with a relative error of $\sim 6\%$.

6. Discussion

The proposed model predicted the temperature history with the highest and the lowest accuracy of < 1°C and ~ 10°C at the 27 selected points, except for points 4 and 7 where the highest discrepancy was of ~ 24°C. At points #4 and 7, we were unable to quantitatively predict the cooling rate at the middle section of the curves (Figures 11(b) and 11(c)). Since these points are in direct contact with the bed, we were not able to consider equivalent points at other layers as they represent filament to filament contact. Nevertheless, the points with the same x_1 and x_2 coordinates at other layers are $\#13, 16, 22, 25$ in which we successfully predicted thermal fields quantitatively. The discrepancy at points 4 and 7 might come from the literature-based thermal properties that

may deviate from the actual values and from the assumption that the surrounding temperature and the air speed were constant at all times during deposition phase. Moreover, since the FEM simulation predicted higher cooling rate for both cases, the discrepancy could be explained by the local increase in the surrounding temperature and/or decrease of the air speed as a result of a slower nozzle movement around the corner which was observed in the G-code data.

When compared the temperature fields on the surface of the layers (Figure 12(b)), the majority of predictions showed the discrepancy of no more than $\sim 10°C$, except the areas near or at the extruder locations where errors were no more than $\sim 75°C$. The latter error comes from the fact that, according to the G-code, these positions are the extruder's last stop when printing a given layer, where it waits for a bed adjustment before printing the next layer. The IR readings are significantly influenced by the extruder's temperature ($T_e = 210°C$) as it blocks the filament reducing the polymer's exposure to the IR camera. In Figure 11(a), the measurement data for Layer 1 clearly shows that the hottest area width is ~ 1.5 mm and it is almost three times larger than the width of the filament, which from a physical stand point, is rather not realistic given the filament's cooling rate. Moreover, the measurements are always higher than the predictions, which further supports our explanation. Therefore, we consider this data as an outlier which can not be improved with our setting. It explains the reason why when we perform the detailed comparison of the temperature fields we shift the points $\#3, 6, 9, 12, 15, 18, 21$ from the edge by 16 mm.

From the sensitivity analysis it was found that the radiation had negligible influence on the thermal fields prediction for all the considered points. This situation can be explained by the fact that, due to the high speed of the FFF process, the dominated thermal mechanisms were convection and conduction. Also, it was concluded that the bed and the surrounding temperatures had the most impact on the predictions followed by the air speed. Similar results were reported by Costa et al. in [13] who concluded that the convection with the environment and the conduction between adjacent filaments dominate the radiation when the filament's convection is greater than 60 W/m^2K (which is our case). Since the convection with the environment is dominating, it emphasizes the importance of the surrounding temperature. The results of sensitivity study with the decreased values of parameters were not significantly different, by the means of an absolute error, from those with the increased values. At the point #1, the influence from the variation of T_b was deemed to be the greatest among other parameters considered in this study. At the points $\#10, 19$ located at higher layers, the influence from the variation of T_s was found to be dominating. These findings can be explained by the fact that at the point #1 the filament was in a direct contact with the print bed increasing the influence of the conduction between the filament and the print bed (mechanism #3 in Fig. 6) over other thermal mechanisms. In contrast, at higher layers the filament was deposited on the previously extruded PLA increasing the role of the convection from the filament to the surrounding and the conduction between the filament overlays corresponding to the mechanisms #1 and 2 in Fig. 6, respectively.

The simulation quantitatively predicted the maximum distortion and the supports deformation. However, the distribution of distortions was, in some areas, approximated only qualitatively as shown in Figure 14. The discrepancy is, to some extend, related to the equipment sensitivity. The FFF manufactured parts exhibit the regions with small deformations close to the sensitivity of a measuring equipment. Usually, these areas are served to remain the part on the bed during the process. Since among our goals, was to simulate the deposition of the filaments on the bed, we decided not to use a raft layer. To limit the area with small distortions, we tried three different shapes reported in the literature namely trapezoid, zigzag and bridge. However, increasing distortions is not only due to the shape, but a combination with the extruded material and printing parameters. Finally, we chose a widely accepted bridge-like shape for benchmarking the process

simulation. From our prospective, scaling the part will not eliminate the area with small distortions. The discrepancy could also come from the simplified mechanical constitutive models that were based on an extrapolation of properties evolution found in the literature on experimentally measured properties at room temperature (see Section 3 for the details).

7. Conclusions

This work demonstrated the numerical approach to compute process induced temperature distribution and distortion in PLA parts manufactured using the FFF process. The procedure combined experimentally measured process parameters and experimentally verified thermal and mechanical steps of the simulation.

It was shown that the temperature fields can be simulated with a satisfactory level of accuracy by using an available literature data on the thermal properties of PLA, by assuming the surrounding temperature and the air speed as homogeneous fields, and by computing process parameters using measured data. It was demonstrated that for the considered tool-path and the speed of the nozzle, the bed and the surrounding temperatures had the most impact on the predictions followed by the air speed.

This work revealed that our procedure yielded qualitative and, in some cases, quantitative predictions of the process-induced geometrical distortions. We used literature data to decrease the mechanical properties measured at the room temperature which turned out to be insufficient to reach the quantitative level of mechanical predictions at all measured data points. To reach a higher level of accuracy a detailed characterization of a temperature-depended mechanical properties as well as relaxation mechanisms of PLA is required.

Thanks to the generality of the developed simulation approach, it can further be applied for a sensitivity analysis to estimate the influence of variation in process parameters such as the nozzle speed and the tool-path on the computed distortion of various polymers and polymer-based composites. Potentially, such a physics-based simulations may train machine learning algorithms to learn the underlying physics of the problem stimulating an efficient analysis of a massive set of parameters to find the optimum combination.

8. Acknowledgment

We acknowledge the support of Safran S.A., and the the Natural Sciences and Engineering Research Council of Canada (NSERC) (CRDPJ514761-17)

We acknowledge Mr. Paul Gregorio a member of the Laboratory for Multiscale Mechanics (LM^2) who helped with the distortion measurements.

We acknowledge Mr. Olivier Duchesne a member of the LM^2 who performed the tensile tests.

9. Dedication

Anton Trofimov dedicates this work to his mentor, colleague and friend Prof. Igor Sevostianov who tragically passed way on August 3rd, 2021.

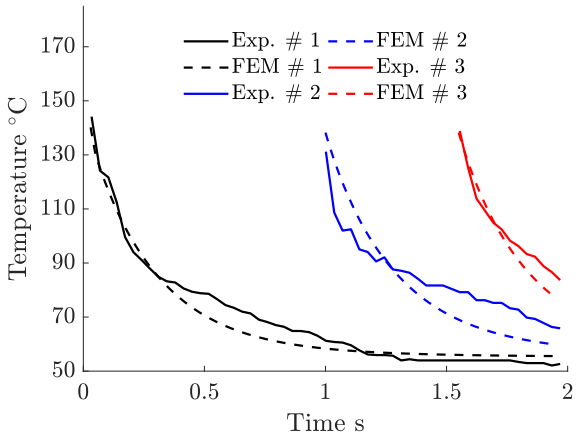
Exp. # 1
FEM # 2
FEM # 1
Exp. # 3
Exp. # 2
FEM # 3
Temperature °C
Time s

(a)

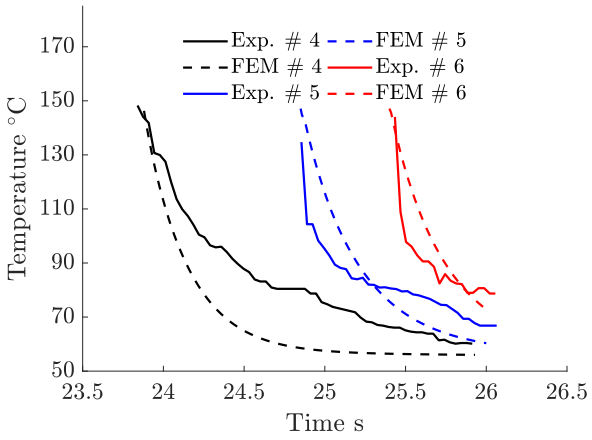
Exp. # 4
FEM # 5
FEM # 4
Exp. # 6
Exp. # 5
FEM # 6
Temperature °C
Time s

(b)

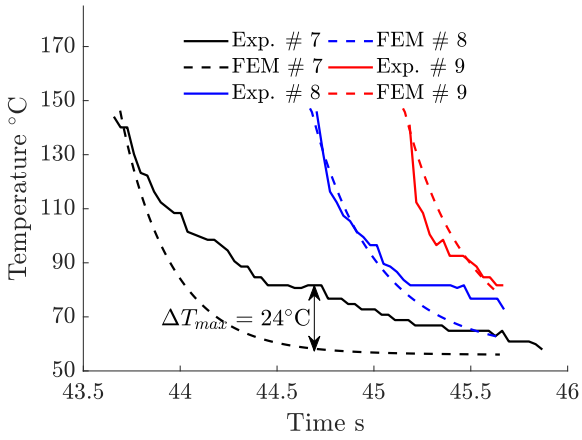
Exp. # 7
FEM # 8
FEM # 7
Exp. # 9
Exp. # 8
FEM # 9
$\Delta T_{max} = 24°C$
Temperature °C
Time s

(c)

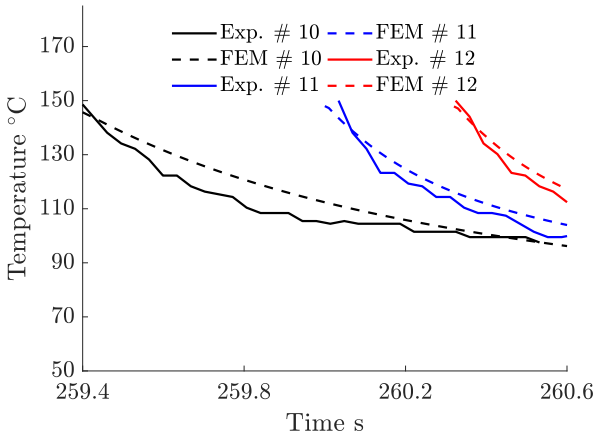
Exp. # 10
FEM # 11
FEM # 10
Exp. # 12
Exp. # 11
FEM # 12
Temperature °C
Time s

(d)

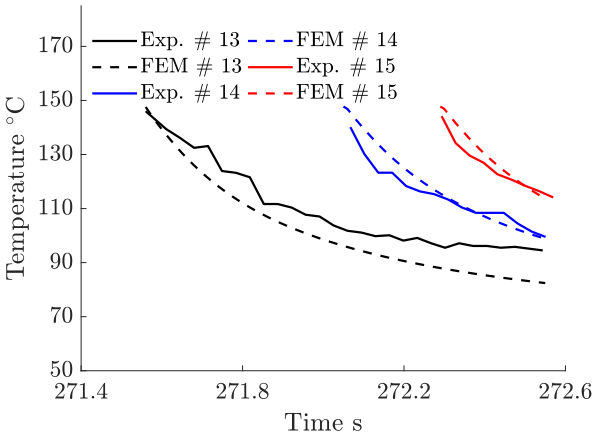
Exp. # 13
FEM # 14
FEM # 13
Exp. # 15
Exp. # 14
FEM # 15
Temperature °C
Time s

(e)

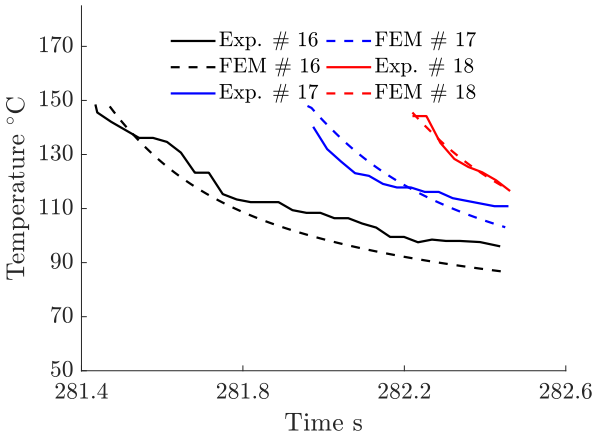
Exp. # 16
FEM # 17
FEM # 16
Exp. # 18
Exp. # 17
FEM # 18
Temperature °C
Time s

(f)

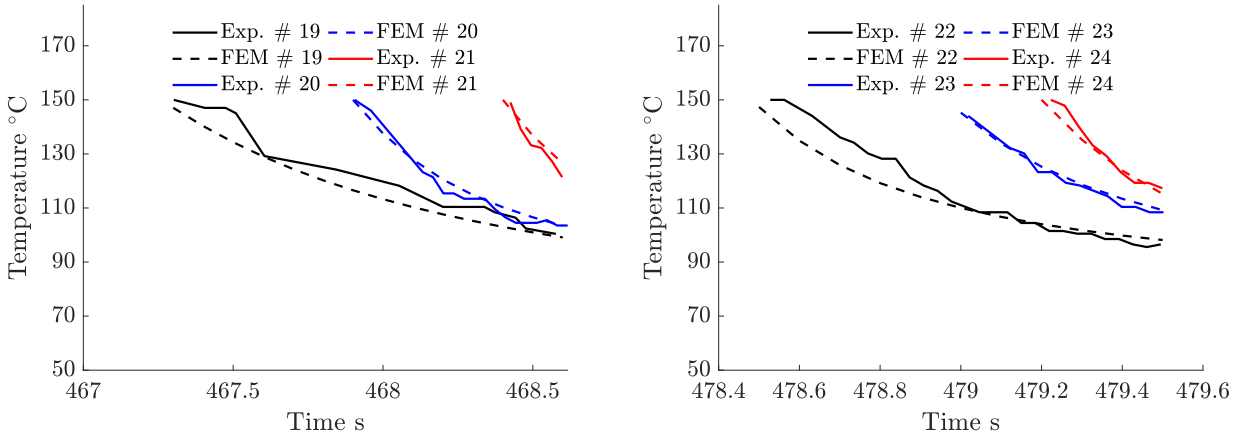

(g)

(h)

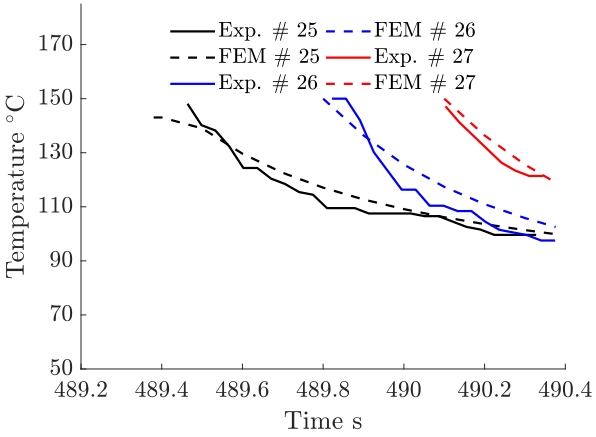

(i)

Figure 11: Comparison between the temperature distribution computed numerically and that experimentally measured at the points # shown in Figure 10 during the FFF process of the regular geometry shown in Figure 4(a): (a) Layer 1, points 1-3; (b) Layer 1, points 4-6; (c) Layer 1, points 7-9 with the highlighted maximum temperature difference among all considered data points discrepancy; (d) Layer 10, points 10-12; (e) Layer 10, points 13-15; (f) Layer 10, points 16-18; (g) Layer 20, points 19-21; (h) Layer 20, points 22-24; (i) Layer 20, points 25-27. Note that, since the first layer deposition speed was almost half as compared to the rest of layers (see Section 3.1) the time span on the Figures 11(a-c) is larger than on the Figures 11(d-k).

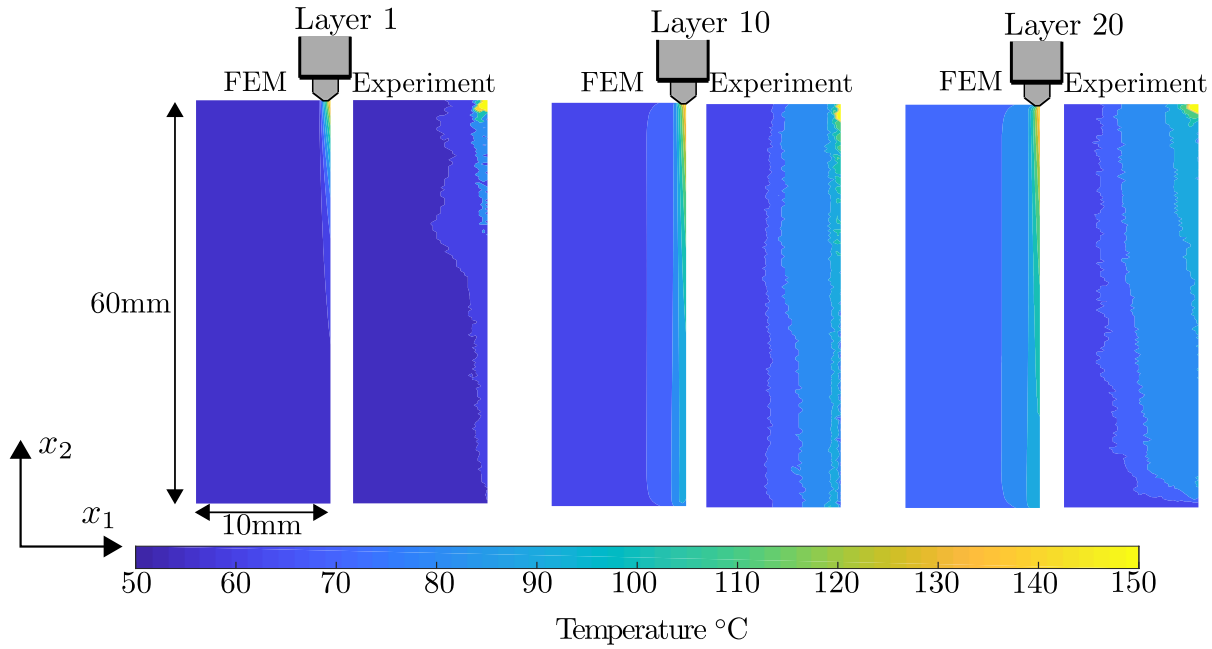

(a)

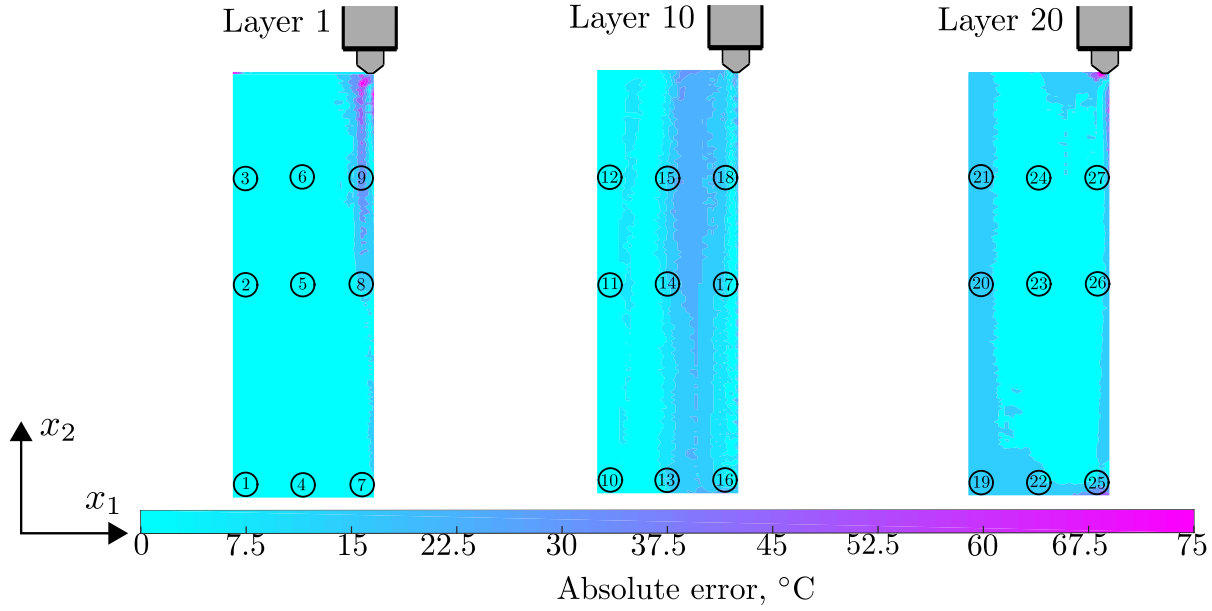

(b)

Figure 12: Comparison of the temperature distribution computed numerically against that experimentally measured at the end of deposition of the first, the tenth (middle) and the twentieth (last) layers.

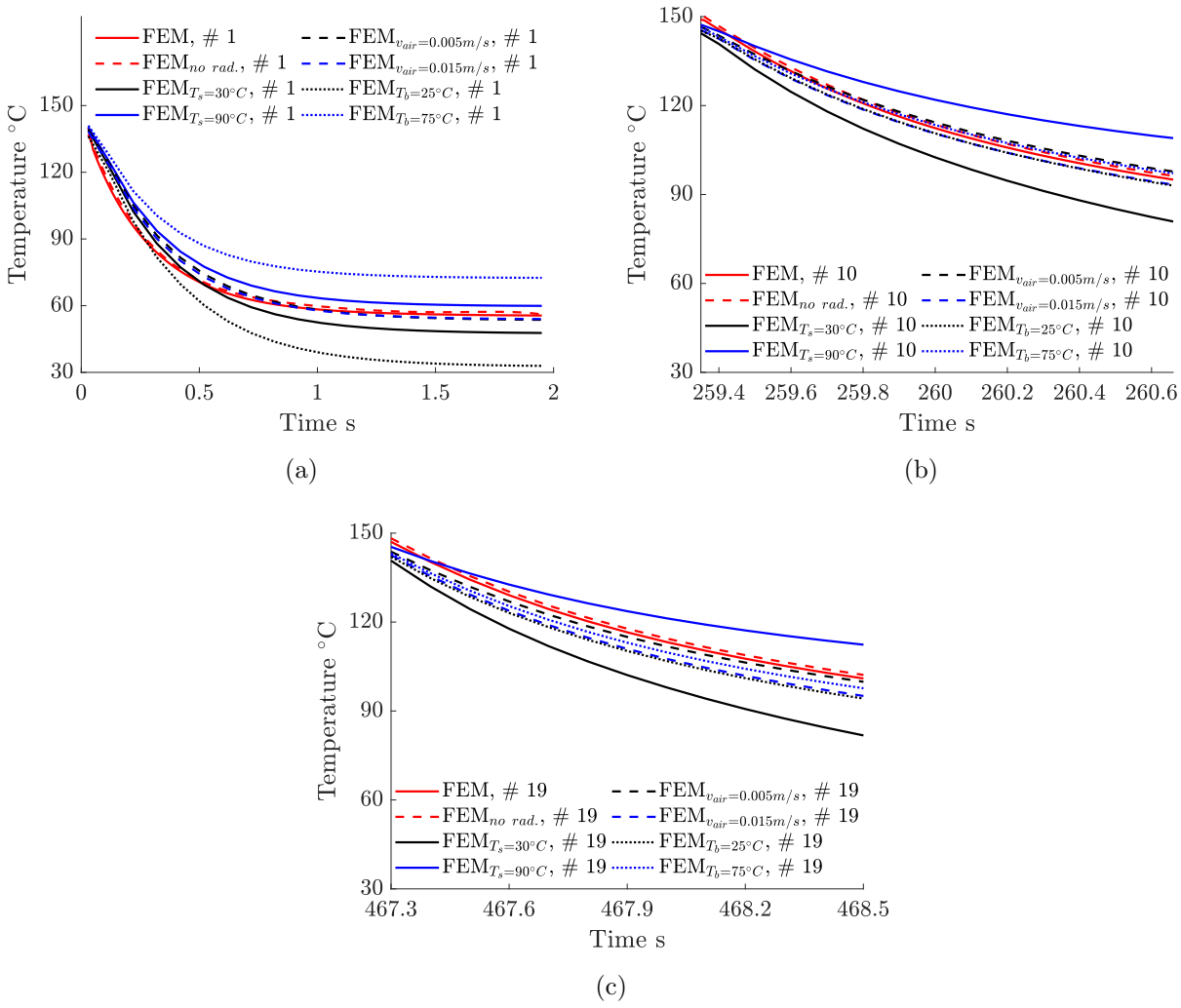

Figure 13: Comparison between the thermal fields computed using process parameters from Table 2 and those simulated using process parameters assumed in the sensitivity study at the points #1, 10, 19 shown in Figure 10 during the FFF process of the regular geometry shown in Figure 4(a): (a) Layer 1, point 1; (b) Layer 10, point 10; (c) Layer 20, point 19.

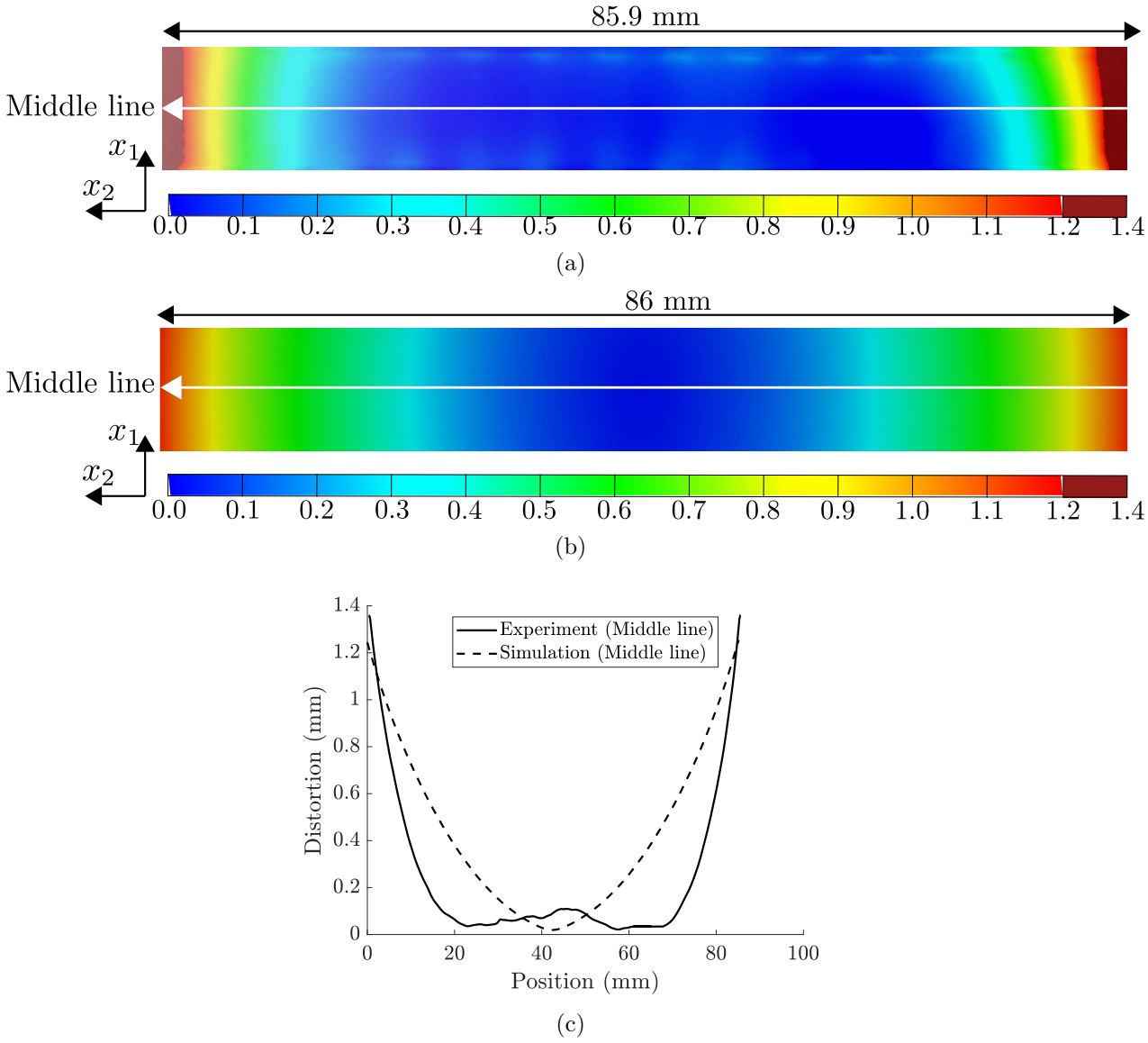

Figure 14: Distortion (mm) contour plots obtained from: (a) the actual FFF manufacturing and subsequent measurements and (b) our simulation procedure; (c) the detailed comparison of the distortion distribution along the Middle line indicated on the Figures (a) and (b).

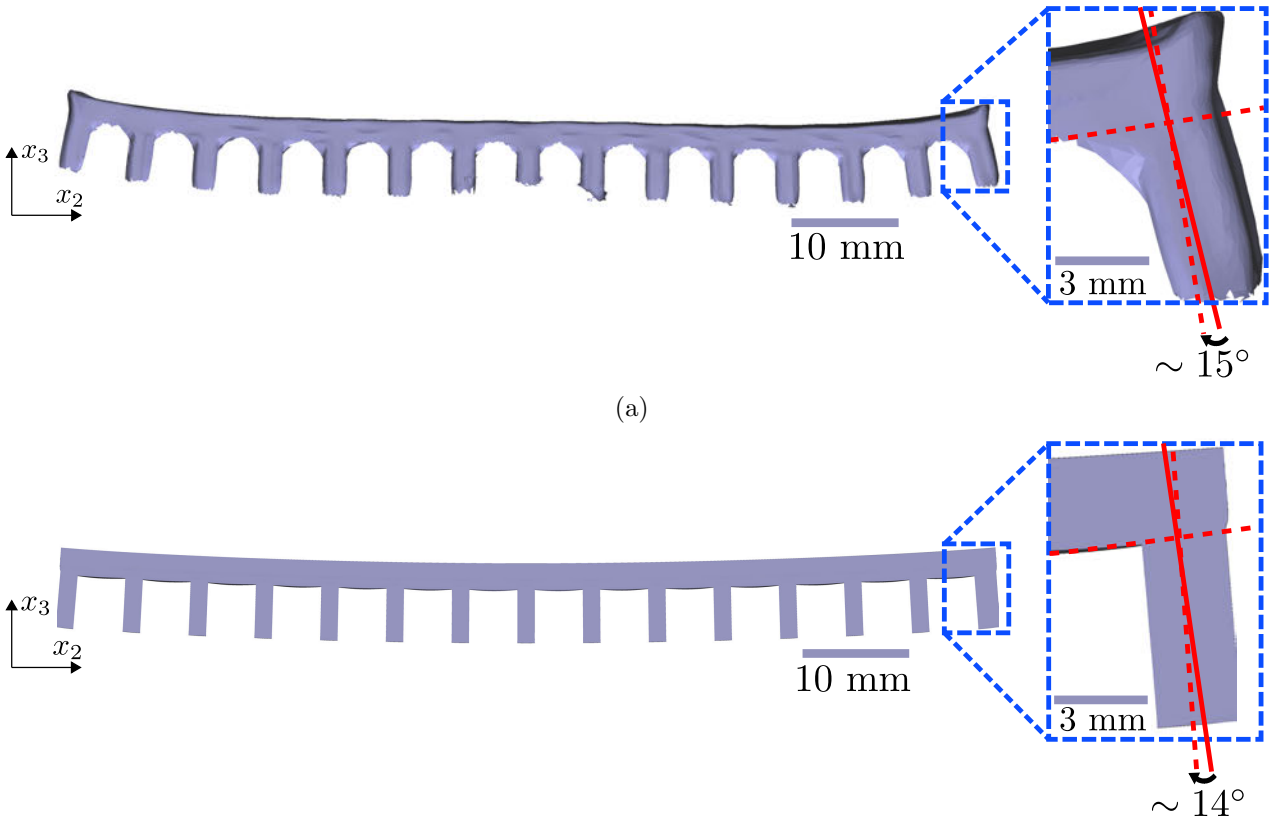

Figure 15: Distortion and the closeup view of support deformation obtained from: (a) the actual FFF manufacturing and subsequent measurements and (b) our simulation procedure. The closeup views show the deviation of the support from being perpendicular to the deck

Appendix A. Details on the computation of the print bed properties

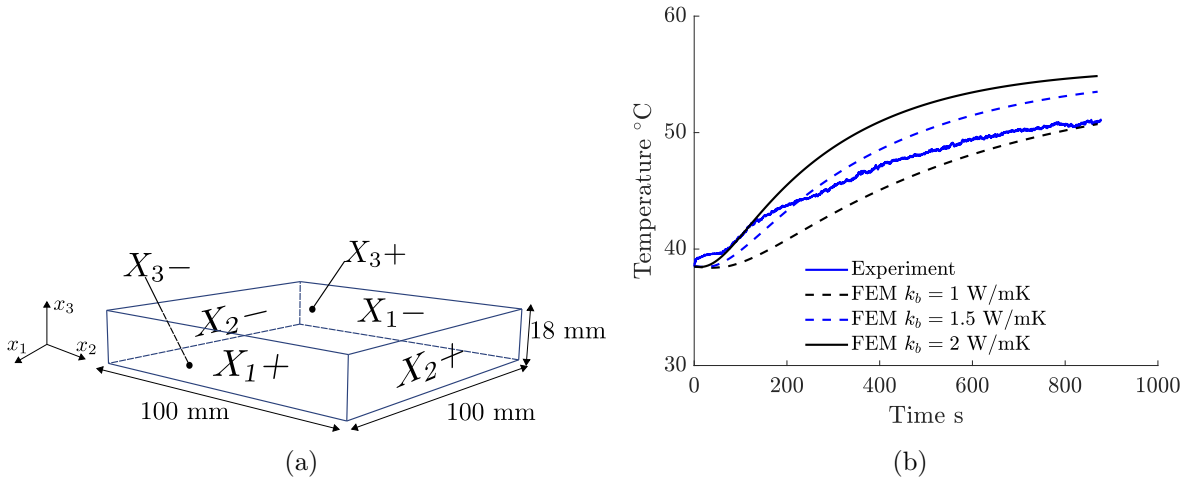

Figure A.1: Comparison of the measured temperature evolution on the surface of the print bed during heating against that computed with FEM. It was deemed that $k_b = 1.5$ W/mmK gives sufficiently accurate predictions.

The Raise3D Pro2 printer print bed consists of several layers that include flexible plate allowing for a better part detachment and the heating elements being at the bottom. We programmed the Raise3D Pro2 printer to heat the print bed from 40° C to 60° C and measured the temperature evolution on the surface using the IR camera which was then averaged over the captured area. Due to the thermal losses and the layered structure, the maximum temperature of the bed was found to be $T_b = 52°$ C. To identify the thermal properties, we best-fitted the experimentally observed thermal evolution during heating with FEM simulations.

Figure A.1(a) presents the geometry of the simulated print bed. In the FEM heat transfer model, the print bed was simulated as a homogeneous rectangular plate and discretized with 1 600 linear 8-node brick elements (DC3D8). The c_p^b and ρ_b were fixed to the values of steel (see Table 1) while k_b was varied to fit the experimental data. The initial measured temperature was 38.5° C. The surrounding temperature was set to 25°C. The boundary conditions included: (1) convection to the surrounding with $h_b = 5.18$ W/mK (computed in Section 4.1) and (2) the constant temperature of 60°C at the bottom surface (X_3- in Figure A.1(a)) of the print bed.

We performed three thermal simulations with $k_b = 1, 1.5$ and 2 W/mmK and computed the temperature at the top surface of the bed along x_3 (X_3+ in Figure A.1(a)). Figure A.1(b) shows the comparison of the measured temperature evolution on the surface of the print bed during heating against that computed with FEM. It was deemed that $k_b = 1.5$ W/mmK gives sufficiently accurate predictions.

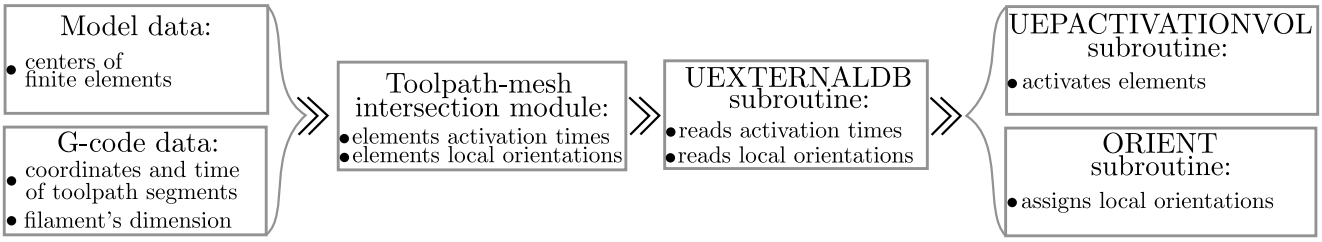

Figure B.2: The workflow inspired from the work of Favaloro et al. [12] implementing the progressive element activation in ABAQUS. ABAQUS' input file containing the coordinates of each finite element's center along with the G-code data containing coordinates of the toolpath and the size of the filament were input to the custom toolpath-mesh intersection module that resulted in the text files with activation times and local orientations. These text files were read at $t = 0$ by ABAQUS' subroutine UEXTERNALDB and the data was forwarded to the subroutines ORIENT that assigns elements' local orientations at the beginning of the analysis and to the UEPACTIVATIONVOL that activates elements with respect to their activation times during the analysis

Appendix B. Details on the FFF process simulation methodology

Figure B.2 presents the workflow inspired from the work of Favaloro et al. [12] implementing the progressive element activation in ABAQUS. ABAQUS' input file containing the coordinates of each finite element's center along with the G-code data containing coordinates of the toolpath and the filament dimensions were input to the custom toolpath-mesh intersection module that resulted in the text files with activation times and local orientations. These text files were read at $t = 0$ by ABAQUS' subroutine UEXTERNALDB and the data was forwarded to the subroutines ORIENT that assigns elements' local orientations at the beginning of the analysis and to the UEPACTIVATIONVOL that activates elements with respect to their activation times during the analysis.

Figure 3(a) illustrates the details of the toolpath-mesh intersection. The toolpath-mesh intersection module starts by extracting the centers of each i-th element ($\mathbf{x}_i^c$, $i = 1, 2...N$, where N is the total number of elements in the system), the elements stacking direction ($\mathbf{x}_i^s$), the filament's width (w_f) and thickness (h), the coordinates of toolpath j-th segment's start and end points ($\mathbf{x}_j^A$ and $\mathbf{x}_j^B$, $j = 1, 2...M$, where M is the total number of segments) and their times (t_j^A and t_j^B) from the ABAQUS's input file and the G-code data. Note that the the filament's width and thickness as well as stacking direction were assumed constant throughout the process. For a given $\mathbf{x}_i^c$, we identify the segments that are either inside or intersect the sphere with the radius r assumed as:

$$r = \sqrt{{w_f}^2 + {h_f}^2}. \tag{B.1}$$

For each selected l-th segment, $\mathbf{x}_l^A$, $\mathbf{x}_l^B$ and t_l^A and t_l^B are used to identify the local coordinate system ($\mathbf{x}_{l,1}$, $\mathbf{x}_{l,2}$, $\mathbf{x}_{j,3}$) of the segment as:

$$\mathbf{x}_{l,1} = \frac{\mathbf{x}_l^B - \mathbf{x}_l^A}{L^{AB}}, \tag{B.2a}$$

$$\mathbf{x}_{l,2} = \frac{\mathbf{x}_i^s \times \mathbf{x}_{l,1}}{||\mathbf{x}_i^s \times \mathbf{x}_{l,1}||}, \tag{B.2b}$$

$$\mathbf{x}_{l,3} = \mathbf{x}_i^s, \tag{B.2c}$$

where $L^{AB} = ||\mathbf{x}_l^B - \mathbf{x}_l^A||$ is the segment's length, $||\cdots||$ is the Euclidean norm. The i-th element's center coordinates $\mathbf{x}_i^{c,segm} = \left(x_{i,1}^{c,segm}, x_{i,2}^{c,segm}, x_{i,3}^{c,segm}\right)$ are then recomputed in terms of the local orientation of the l-th segment as:

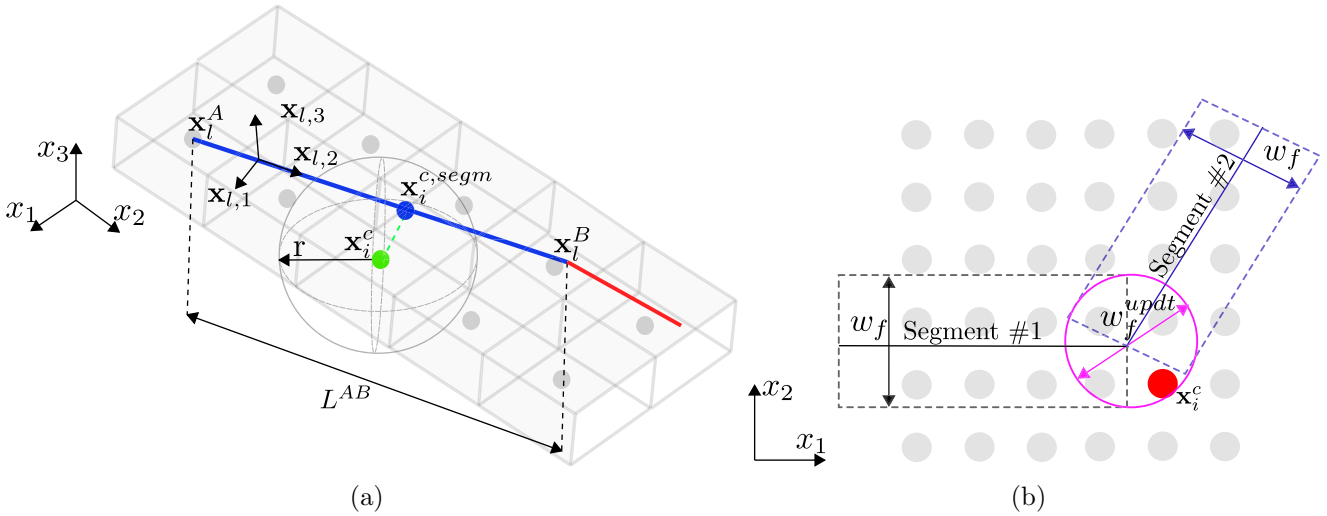

Figure B.3: The details of the toolpath-mesh intersection module computational procedure. Figure (a) illustrates the center point (marked in green) of the i-th element at which the search for the segments that either inside or intersect the sphere with the radius r was conducted. It shows that the segment AB (marked in blue) intersects the sphere and, thus, the center point was projected on it (projection was marked in blue) to compute the activation time of the i-th element. Figure (b) illustrates an example of the i-th center point (marked in red) located close to the tip of the two segments (marked in blue and black) and that can be missed by the two searching steps due to the piece-wise nature of the segments. Therefore, an additional search within the area marked by the magenta circle is required

$$x_{i,1}^{c,segm} = (\mathbf{x}_i^c - \mathbf{x}_l^A) \cdot \mathbf{x}_{l,1}, \tag{B.3a}$$

$$x_{i,2}^{c,segm} = (\mathbf{x}_i^c - \mathbf{x}_l^A) \cdot \mathbf{x}_{l,2}, \tag{B.3b}$$

$$x_{i,3}^{c,segm} = (\mathbf{x}_i^c - \mathbf{x}_l^A) \cdot \mathbf{x}_{l,3}. \tag{B.3c}$$

The location of the i-th element center with respect to the l-th segment can be characterized as:

- if $x_{i,1}^{c,segm} < 0$ or $x_{i,1}^{c,segm} > L^{AB} + w_f/2$ - the element's center is outside the j-th filament and the i-th element must not be activated;
- if $0 \leq x_{i,1}^{c,segm} < L^{AB}$ and $|x_{i,2}^{c,segm}| \leq w_f/2$ and $0 \leq x_{i,3}^{c,segm} \leq h$ - the element's center is inside the j-th filament and the i-th element must be activated;
- if $L^{AB} \leq x_{i,1}^{c,segm} \leq L^{AB} + w_f/2$ - the element's center might be missed by previous search (see Fig. 3(a)(b)). The updated width $w^{updt} = \sqrt{(w_f)^2 - 4(x_{i,1}^{c,segm} - L^{AB})^2}$ is used. If $|x_{i,2}^{c,segm}| \leq w_f^{updt}/2$, and $0 \leq x_{i,3}^{c,segm} \leq h$ - the element's center is inside the j-th filament and the i-th element must be activated.

When the i-th element's center is considered to be inside the filament then its activation time is computed as:

$$t_i^{act} = t^A + \frac{(t^B - t^A)x_{i,1}^{c,segm}}{L^{AB}}. \tag{B.4}$$

References

[1] P. Parandoush, D. Lin, A review on additive manufacturing of polymer-fiber composites, Composite Structures 182 (2017) 36–53. doi:10.1016/j.compstruct.2017.08.088.

[2] A. Jaisingh Sheoran, H. Kumar, Fused Deposition modeling process parameters optimization and effect on mechanical properties and part quality: Review and reflection on present research, Materials Today: Proceedings 21 (2020) 1659–1672. doi:10.1016/j.matpr.2019.11.296.

[3] A. Armillotta, M. Bellotti, M. Cavallaro, Warpage of FDM parts: Experimental tests and analytic model, Robotics and Computer-Integrated Manufacturing 50 (2018) 140–152. doi:10.1016/j.rcim.2017.09.007.

[4] Z. Hu, S. Mahadevan, Uncertainty quantification and management in additive manufacturing: current status, needs, and opportunities, The International Journal of Advanced Manufacturing Technology 93 (5-8) (2017) 2855–2874. doi:10.1007/s00170-017-0703-5.

[5] F. Ning, W. Cong, Y. Hu, H. Wang, Additive manufacturing of carbon fiber-reinforced plastic composites using fused deposition modeling: Effects of process parameters on tensile properties, Journal of Composite Materials 51 (4) (2017) 451–462. doi:10.1177/0021998316646169.

[6] B. Brenken, E. Barocio, A. Favaloro, V. Kunc, R. B. Pipes, Fused filament fabrication of fiber-reinforced polymers: A review, Additive Manufacturing 21 (2018) 1–16. doi:10.1016/j.addma.2018.01.002.

[7] Y. Zhang, Y. Chou, Three-dimensional finite element analysis simulations of the fused deposition modelling process, Proceedings of the Institution of Mechanical Engineers, Part B: Journal of Engineering Manufacture 220 (10) (2006) 1663–1671. doi:10.1243/09544054JEM572.

[8] Y. Zhang, K. Chou, A parametric study of part distortions in fused deposition modelling using three-dimensional finite element analysis, Proceedings of the Institution of Mechanical Engineers, Part B: Journal of Engineering Manufacture 222 (8) (2008) 959–968. doi:10.1243/09544054JEM990.

[9] A. Cattenone, S. Morganti, G. Alaimo, F. Auricchio, Finite Element Analysis of Additive Manufacturing Based on Fused Deposition Modeling: Distortions Prediction and Comparison With Experimental Data, Journal of Manufacturing Science and Engineering 141 (1) (jan 2019). doi:10.1115/1.4041626.

[10] B. Courter, V. Savane, J. Bi, S. Dev, C. Hansen, Finite Element Simulation of the Fused Deposition Modelling Process, in: NAFEMS World Congress, 2017, pp. 11–14.

[11] E. Barocio, B. Brenken, A. Favaloro, M. Bogdanor, R. B. Pipes, Extrusion deposition additive manufacturing with fiber-reinforced thermoplastic polymers, in: Structure and Properties of Additive Manufactured Polymer Components, Elsevier, 2020, pp. 191–219. doi:10.1016/B978-0-12-819535-2.00007-7.

[12] A. J. Favaloro, E. Barocio, B. Brenken, R. B. Pipes, E. Barocio, R. B. Pipes, Simulation of Polymeric Composites Additive Manufacturing using Abaqus, in: Dassault Systemes' Science in the Age of Experience, no. May, Chicago, 2017, pp. 103–114.

[13] S. Costa, F. Duarte, J. Covas, Thermal conditions affecting heat transfer in FDM/FFE: a contribution towards the numerical modelling of the process, Virtual and Physical Prototyping 10 (1) (2015) 35–46. doi:10.1080/17452759.2014.984042.

[14] H. Carslaw, J. Jaeger, Conduction of heat in solids, 2nd Edition, Oxford University Press, New York, 1959.

[15] S. Farah, D. G. Anderson, R. Langer, Physical and mechanical properties of PLA, and their functions in widespread applications — A comprehensive review, Advanced Drug Delivery Reviews 107 (2016) 367–392. doi:10.1016/j.addr.2016.06.012.

[16] Raise3D, Raise3D Premium PLA Technical Data Sheet (2019).

[17] H. Prajapati, D. Ravoori, A. Jain, Measurement and modeling of filament temperature distribution in the standoff gap between nozzle and bed in polymer-based additive manufacturing, Additive Manufacturing 24 (2018) 224–231. doi:10.1016/j.addma.2018.09.030.

[18] A. Bejan, Heat Transfer, John Wiley & Sons, Inc., New York, 1993.

[19] S. F. Costa, F. M. Duarte, J. A. Covas, Estimation of filament temperature and adhesion development in fused deposition techniques, Journal of Materials Processing Technology 245 (2017) 167–179. doi:10.1016/j.jmatprotec.2017.02.026.

[20] Y. Touloukian, P. Liley, S. Saxena, Thermal conductivity: nonmetallic liquids and gases, IFI/Plenum, New York, 1970.

[21] R. Hill, The mathematical theory of plasticity, Vol. 11, Oxford university press, 1998.

[22] F. Espinach, S. Boufi, M. Delgado-Aguilar, F. Julián, P. Mutjé, J. Méndez, Composites from poly(lactic acid) and bleached chemical fibres: Thermal properties, Composites Part B: Engineering 134 (2018) 169–176. doi:10.1016/j.compositesb.2017.09.055.

[23] C. Zhou, H. Guo, J. Li, S. Huang, H. Li, Y. Meng, D. Yu, J. de Claville Christiansen, S. Jiang, Temperature dependence of poly(lactic acid) mechanical properties, RSC Advances 6 (114) (2016) 113762–113772. doi:10.1039/C6RA23610C.

[24] Y. Song, Y. Li, W. Song, K. Yee, K.-Y. Lee, V. Tagarielli, Measurements of the mechanical response of unidirectional 3D-printed PLA, Materials & Design 123 (2017) 154–164. doi:10.1016/j.matdes.2017.03.051.

[25] J. Keenan, J. Chao, J. Kaye, Gas Tables-International Version, 2nd Edition, John Wiley & Sons, New York, NY, 1983.

[26] Landolt-Börnstein, Units and Fundamental Constants in Physics and Chemistry, Springer-Verlag Berlin Heidelberg, 1991.